FINE-SCALE STRUCTURE OF THE NEUTRAL HYDROGEN ABSORPTION IN NGC1275

Thesis by

Jonathan Daniel MacLeish Romney

In Partial Fulfillment of the Requirements

for the Degree of

Doctor of Philosophy

California Institute of Technology

Pasadena, California

1979

(Submitted 1978 June 21)

ACKNOWLEDGEMENTS

Only those who have experienced the catharsis of writing a thesis can understand the heartfelt thanks expressed by the authors in their Acknowledgements. I am indeed glad to be able, finally, to record my gratitude to a few of the many who have aided, guided, and supported me throughout this experience.

My academic mentor in this venture has been Marshall Cohen, whose approach to advising me has been well adapted to my temperament, and, I suspect, at times a strain upon his. His ability to offer persistent, sometimes insistent, encouragement and guidance while preserving for me the opportunities to go my own way, and learn from my frequent mistakes, has been remarkable. Other major contributors to my academic growth have included Dave Jauncey, Sam Gulkis, and, especially, Alan Moffet, who introduced me to radio astronomy when I was a Caltech freshman.

Very-long-baseline interferometry is a labor-intensive form of astronomy, and it has been my good fortune to have had the diligent assistance of a number of colleagues during the observations on which this thesis is based. Ivan Pauliny-Toth and Eugen Preuss in Bonn were most thorough in smoothing the way for observations at a

telescope with which I was unfamiliar, and in providing a variety of explicit calibration information, and Dave Shaffer in Green Bank saved most of the experiment by his early discovery of an unlocked oscillator. In two preliminary experiments not reported here, I was fortunate to be helped by George Purcell, who drove to Green Bank in a snowstorm, by Tony Readhead, Richard Schilizzi, and Peter Wilkinson, who moved their Brit Thanksgiving to Owens Valley, and by Nan Dieter and Jack Welch, who re-invented the digital clock for me at Hat Creek. I am further indebted to the staffs of the several observatories, and in particular to Harry Hardebeck at Owens Valley and Joe Burch in Charlottesville.

A long and tedious numerical path connects the Mark II processor output to the maps and graphs presented here. Much of the software paving that path grew out of discussions with Mark Reid while we were both learning the intricacies of VLBI line work. Near the end of the path I was fortunate to find a freeway in the form of the CLEAN system as adapted for VLBI use by Marshall Cohen, Tony Readhead, and Peter Wilkinson.

In interpreting my observations I have benefitted greatly from numerous discussions with Steve Kent, another NGC1275 freak. I am happy also to acknowledge helpful discussions on various aspects of this project with Drs.

Roger Angel, Geoffrey Burbidge, Jill Knapp, George Miley, Alan Moffet, and Tony Readhead, among others. Dr. W. K. Ford, Jr., kindly sent me a preprint of the "RFPO" paper.

During part of my tenure as a graduate student at Caltech, I was supported by a National Science Foundation Graduate Fellowship, for which I thank the Foundation. The hospitality of the National Radio Astronomy Observatory, and of the Institute of Astronomy at Cambridge University are acknowledged with thanks. And to Gordon Stanley and Alan Moffet, the former and present Directors of the Owens Valley Radio Observatory, I am grateful for supporting much of the extensive computing required for this project.

My two recent officemates in Room 9A, Anneila Sargent and Menachem Cimerman, have participated in the completion of this thesis more deeply than they may have wished. It is pleasant indeed to thank them for their good companionship as well as their patience.

I have looked forward a very long time to being able to acknowledge today the aid and comfort offered me by my partner, Valerie. Her contributions to this thesis range from editorial assistance and typing, to remaining always an honest human contact, even during the recent months and weeks when I have at times been obsessed with the many major and minor points that "just don't make sense". I am happy to have had her share this part of my life.

ABSTRACT

The high-velocity 21-cm absorption feature in NGC1275 (=3C84) has been mapped at an angular resolution of a few milliarcseconds with an intercontinental very-long-baseline interferometer. The method of analysis makes use of both the absolute amplitude of the visibility function in the continuum, and the relative amplitude and phase between the line and continuum.

Fine-scale structure in the continuum is determined from the observations, and the 21-cm structure of 3C84 on angular scales covering almost six orders of magnitude is reviewed.

The HI absorption is found to arise in a cloud covering part of the intense, compact continuum nucleus. Although absorption is seen against the brightest part of the continuum structure, the cloud is displaced to the northeast from the nucleus, reaching optical depths of at least 0.83. The cloud is at least 5.6 pc in diameter, with a deduced volume density between 12 and 120 cm^{-3}.

Two basic hypotheses which have been advanced to elucidate the 21-cm absorption and other high-velocity features in NGC1275 are discussed. The results of the

present investigation strongly support the interpretation that all the high-velocity features arise in a superposed galaxy in the Perseus Cluster. The alternative model, in which the high-velocity gas is ejected from the active nucleus, is inconsistent with the structure observed in the HI absorption.

TABLE OF CONTENTS

I. INTRODUCTION

The nature of the peculiar galaxy NGC1275 has long been the object of investigation and controversy. Its singular optical features betoken profound activity, and the associated radio source (Per A = 3C84 = NRAO132) is one of the most complex known. Two especially enigmatic features are the presence of components at two widely separated velocities, discovered by Minkowski (1957), and the remarkable extended network of bright filaments. One of the two velocity components, $\sim$ 5200 km s^{-1}, is close to the mean within the Perseus Cluster, and is generally taken to be the systemic velocity of NGC1275; Lynds (1970) has shown that the line emission from the filamentary structure occurs only at this velocity.

The origin of the high-velocity component, at $\sim$ 8200 km s^{-1}, has been controversial. In Minkowski's (1957) interpretation, the high-velocity lines arise in a second galaxy which is colliding with NGC1275. From their mapping of both components of the velocity field, Burbidge and Burbidge (1965) suggested instead that the high-velocity gas has been ejected from the active nucleus of the galaxy. This interpretation seems to have been generally accepted until the discovery by DeYoung, Roberts, and

Saslaw (1973) of 21-cm absorption in 3C84, covering a narrow range of velocities near 8120 km s^{-1}. These authors considered an interpretation involving absorption in a superposed member of the Perseus Cluster, as well as detailed models in which the absorbing gas is ejected from NGC1275 at constant velocity. Synthesis observations by Ekers, van der Hulst, and Miley (1976) showed the absorbing region to be smaller than a few arcseconds in extent, and centered to within 1" on the nuclear continuum source. More recent discussions (Shields and Oke 1975; Oort 1976; Rubin, Ford, Peterson, and Oort 1977) have adduced abundant evidence for the superposed-galaxy hypothesis, although Adams (1976) has put forward again the suggestion that the galaxies are colliding, while Burbidge, Smith, and Burbidge (1978) consider the ejection hypothesis more natural. Van den Bergh (1977) has concluded that none of these interpretations is completely satisfactory.

The ejection and the superposition (or collision) hypotheses predict differently the appearance of the absorption structure against the fine-scale continuum nucleus. In this paper we present maps of the 21-cm absorption structure in 3C84 at an angular resolution of a few milliarcseconds. The observation and reduction procedures are described in §II; in §III we outline the analysis of the reduced data and present the results. The

two major hypotheses on the nature of NGC1275, and the significance thereto of the observational results, are discussed in §IV, and the conclusions summarized in §V.

II. OBSERVATIONS AND REDUCTION

On 1975 December 4-5, a complete apparition of 3C84 was observed at the frequency of the redshifted HI absorption feature (1.38 GHz) with an intercontinental very-long-baseline array consisting of the 100-meter telescope of the Max-Planck-Institut für Radioastronomie (MPIR) at Effelsberg, Federal Republic of Germany; the 43-meter telescope of the National Radio Astronomy Observatory (NRAO), at Green Bank, West Virginia, U.S.A.; and the 40-meter telescope of the Owens Valley Radio Observatory (OVRO), at Big Pine, California, U.S.A. Typical operating parameters of the three telescopes are given in Table 1. These stations form three predominantly east-west baselines with lengths in the approximate ratios of 1:2:2.5; the use of altazimuth telescopes at both ends of the array allows advantageous coverage in the (u, v) plane, as shown in Figure 1. The antenna feeds received radiation linearly polarized in position angle 0°. The observed signals were recorded at each station using the NRAO Mark II VLBI system.

The independent local oscillators were derived from hydrogen-maser standards at NRAO and OVRO, and from a rubidium-vapor standard at MPIR. An rf band 250 kHz wide

TABLE 1

TELESCOPE PARAMETERS

Station	System Noise Temperature (K)	Aperture Efficiency
MPIR	111	0.55
NRAO	99	0.39
OVRO	92	0.56

Figure 1 - Loci of the baseline vectors as projected onto the sky in the direction of 3C84. Data described in the text were obtained along the solid portions of the curves. The projected vectors are resolved into components pointing east (U) and north (V); axis graduations are in units of millions of wavelengths. Only the positive-U half-plane is shown because the function sampled is Hermitian. The + symbols mark integral values of the interferometer hour angles along the curves.

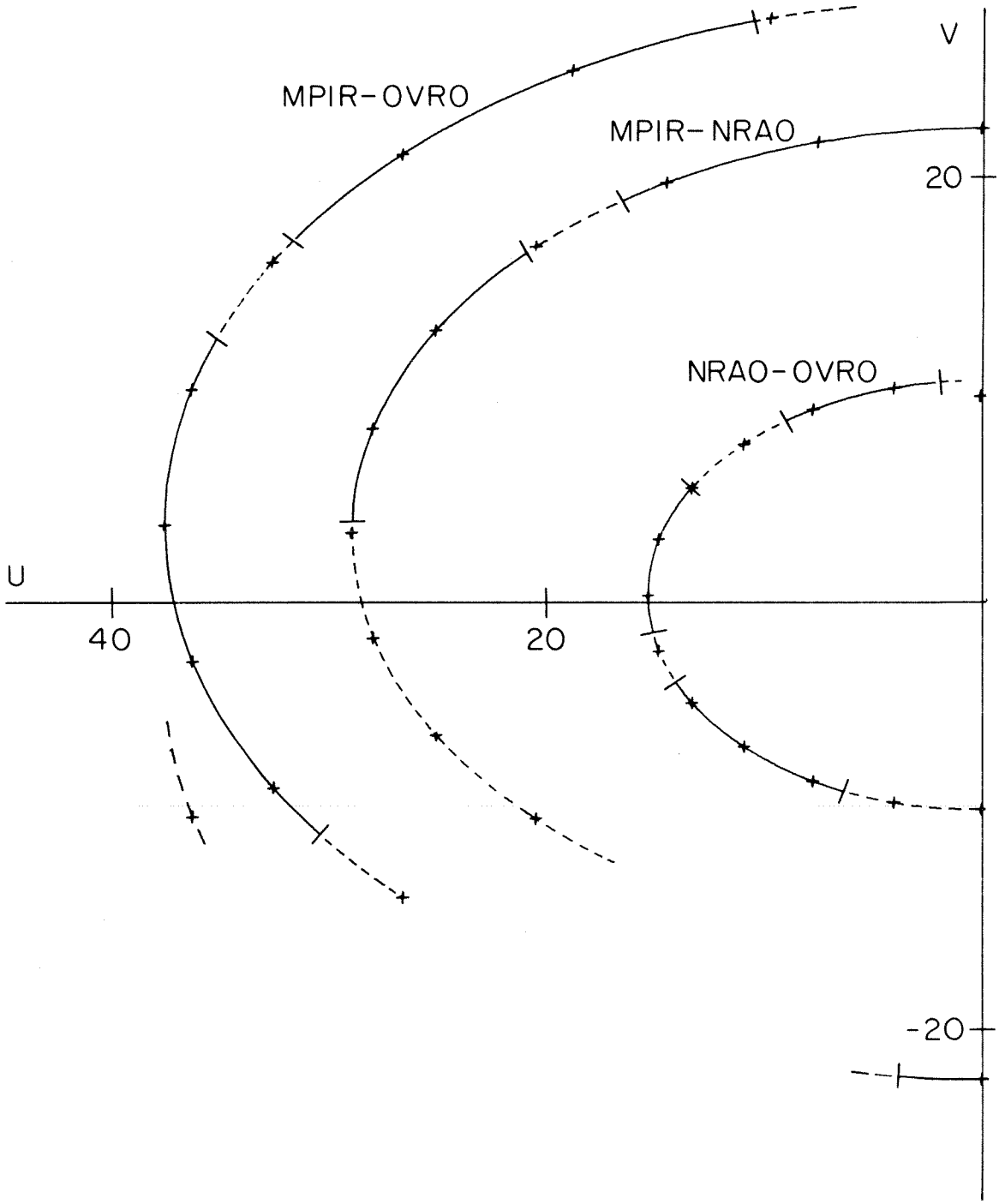
V
MPIR-OVRO
MPIR-NRAO
20
NRAO-OVRO
U
40
20
-20

was centered on the absorption feature at 8114 km s^{-1}; [1] all three local oscillators were adjusted periodically to track the frequency of this feature as seen at NRAO, the central station, thus retaining constant minor offsets between the three oscillators. The accuracy of this tracking was within 200 Hz, which is less than a tenth of a channel at the highest resolution used.

3C84 was observed in a 30-minute cycle consisting of a 25-minute phase with the antennas pointed at the source, followed by a 5-minute off-source phase. The local oscillator synthesizers were adjusted, when necessary, between cycles. Three hours of data were spoiled at NRAO by an unlocked local oscillator; further loss of data was caused by occasional episodes of radar interference at MPIR.

Total system temperatures and, at MPIR and OVRO, source antenna temperatures, were monitored hourly. Independent measurements at MPIR (I.I.K. Pauliny-Toth, private communication) and OVRO established the

---

[1] All "velocities" given in this paper are cz, with respect to the sun, where z is the (optical) redshift $(\lambda - \lambda_o)/\lambda_o$. The relativistically correct velocity corresponding to cz = 8114 km s^{-1} is $c\beta$ = 8004 km s^{-1}.

flux of 3C84 at 1.38 GHz as 14.7 ± 0.8 Jy.

The interferometers were completed in the Mark II VLBI Processor at the National Radio Astronomy Observatory in Charlottesville, Virginia. The recorded data were correlated, one baseline at a time, in a processor configuration which yielded a 192-point complex crosscorrelation function, and a 96-point (real, positive) autocorrelation function for each station.

The cross- and autocorrelation data were treated separately in the preliminary post-correlation data reduction. For the crosscorrelation data this processing included weighted vector averaging over 2-second intervals and Fourier transformation (with uniform weighting) into the (video) frequency domain. A frequency-dependent distortion of the cross-correlation amplitude, due to a processor hardware bug (J. Broderick, J. Moran, Private communications), was removed; however, the time- and frequency-dependent "fractional bit-shift" correction was ignored because this effect is insignificant for the narrow bandwidth used here. For the preliminary reduction of the autocorrelation data, the raw data were accumulated for an entire on- or off-source scan before normalizing, applying corrections, and transforming into the frequency domain. Correction for the effect of asymmetric one-bit clipping was accomplished according to a modification,

derived in Appendix A, of the treatment of Van Vleck and Middleton (1966).

Coherent integration and calibration of the cross-correlation data was done twice, following two separate paths corresponding to two different objectives. One path was aimed at producing accurate absolute amplitudes of the complex visibility function for use in determining the angular structure of the continuum emission. For this purpose one must use a short enough integration time to preclude decorrelation of the fringes by frequency-standard phase fluctuations. Conversely, one needs only enough spectral resolution to avoid contamination of the desired continuum by the absorption feature and the band edges; thus the bandwidth-per-channel can be increased to compensate for the short integration time. This reduction in spectral resolution was accomplished by Fourier transforming the spectra, truncating the resulting correlation functions to a smaller maximum lag, and retransforming the truncated correlation functions to produce spectra with fewer points spanning the bandwidth. This procedure is equivalent to, but faster and simpler than, a convolution of the original spectra with a function of the form $(\sin \alpha x)/\alpha x$.

Tests performed on the data from all three baselines

at a variety of integration times and spectral resolutions showed that an integration of 4 minutes produced negligible (less than 2%) decorrelation, and that for this integration time a 24-point spectrum (i.e., channel spacing of 10.42 kHz) allowed both an optimal separation of the continuum from contamination features, and a satisfactorily high signal-to-noise ratio in almost all integrations. In performing these tests, care was taken to include observations made at twilight at the various stations, when ionospheric scintillations are expected to be most deleterious in corrupting the interferometer phase stability.

The other coherent-integration path was optimized toward determining the relative complex visibility function, at high spectral resolution (2.604 kHz channel spacing), for use in mapping the absorption feature relative to the continuum emission, as described in §IIIc. Since interferometer phase fluctuations have the same decorrelating effect at all frequencies in the observed band, the relative visibility function is insensitive to decorrelation. Quite long integrations, limited only by the eventual deterioration of the signal-to-noise ratio, can profitably be used in this case.

In the present observations, a full 25-minute on-

source scan was integrated as one unit; tests showed that this procedure achieved good signal-to-noise, and that the resulting rather coarse spacing in the (u, v) plane - neighboring points are separated by 1/2 hour in interferometer hour angle - did not appreciably distort the relative absorption map.

A novel technique (described in detail in Appendix B) was used in performing the coherent integration used to obtain both the absolute-amplitude and relative-visibility data. After an initial vector average (to 10 and 60 seconds, respectively, for the 4- and 25-minute integrations), the data were fitted by an iterative non-linear least-square algorithm to a three-parameter function

$$\Gamma_\nu(t_i) = A_\nu \exp\,[i(2\pi f_\nu t_i + \phi_\nu)] \qquad (1)$$

in which the parameters A_ν, f_ν, and ϕ_ν are the amplitude, fringe frequency, and phase in the spectral channel denoted by ν ; each channel is fitted independently. As discussed in Appendix B, the least-squares approach offers a number of advantages for accurate estimation of the parameters, and for the function in equation (1) the non-linear problem is quite tractable and can be implemented for rapid computation.

Conventionally, the calibration of spectral VLBI observations is accomplished by the use of single-dish

spectra derived from autocorrelation of the VLBI data, without recourse to auxiliary measurements of receiver parameters (Moran, 1976). This method is based on the fact that the signal available for correlation in the interferometer is the geometric mean of the signals due to the source at the individual antennas; the system noise power, which is not correlated in the interferometer, must be removed from the autocorrelation spectra with the aid of off-source observations. In principle this removal is possible whenever a spectral feature is present, and in the observations of molecular masers both the presence of powerful but narrow emission lines and the absence of a spectral continuum allow this calibration method to be used advantageously. In absorption spectra the situation is less satisfactory: there is no spectral region where the source signal vanishes, and the enormous spectral flux density of the maser lines and the attendant high signal-to-noise ratio are lacking. Both conditions conspire to make difficult the separation of the effects due to system noise and to antenna sensitivity.

These considerations are set forth at greater length in Appendix C, in which the calibration procedure used with the present observations is derived. Essentially, this procedure is a hybrid of the conventional spectral and continuum calibration methods, using both the autocorre-

lation source spectra and auxiliary measurements of the system and (continuum) antenna temperatures. This method was applied separately to the results of both paths of coherent integration.

III. ANALYSIS AND RESULTS

a) Spectra

In an initial reconnaissance of the high-resolution spectra, the amplitude spectra from the calibrated 25-minute integrations were (incoherently) averaged and a linear baseline removed. The result, shown in the upper panel of Figure 2, is approximately the spectrum seen by the synthesized interferometer beam. For comparison, the lower panel of Figure 2 shows the spectrum seen by a single antenna (MPIR), obtained from the on- and off-source autocorrelation data. In both spectra the resolution of 3.14 kHz (0.70 km s^{-1}) is similar to that of DeYoung, Roberts and Saslaw (1973), and corresponding features can be identified.

Parameters of the primary feature at 8114 km s^{-1} are listed in Table 2 for the synthesized-beam and single-antenna spectra; this absorption is analyzed in §IIIc. The secondary feature at 8120 km s^{-1} is clearly visible in the interferometer spectrum, and thus must be seen against the compact structure investigated in §IIIb, but is too weak for further analysis. The position of the absorption causing the weak shoulder near 8107 km s^{-1}, lost within the noise in the interferometer spectrum, is discussed briefly in §IVb.

Figure 2 - Spectra of the HI absorption feature in 3C84, as seen by the synthesized interferometer beam (top) and by a single antenna (bottom). Spectral resolution is 0.70 km s^{-1}; (sin x)/x interpolation is used in drawing the curves. The ordinate scales are normalized to the continuum.

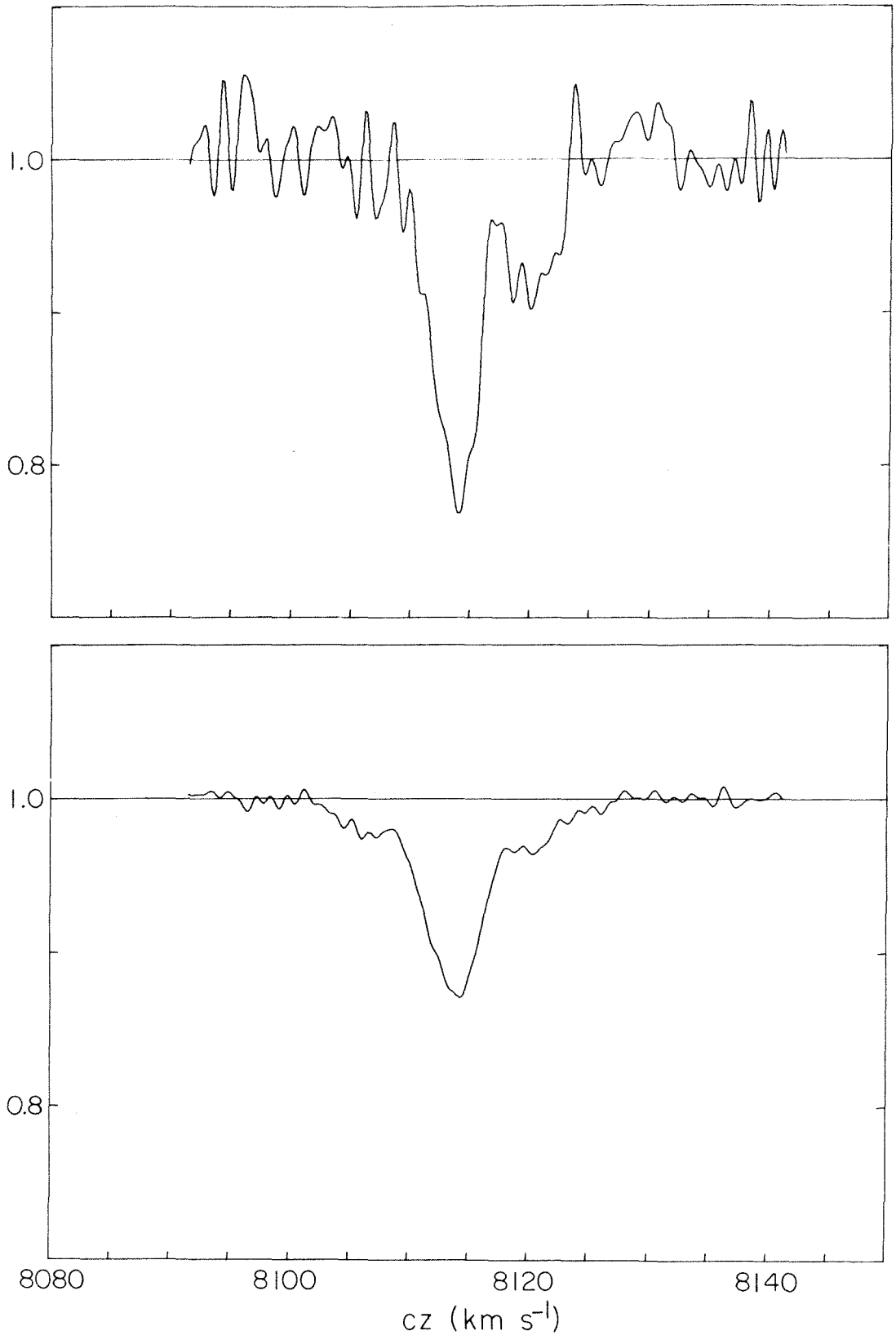
1.0
0.8
1.0
0.8
8080
8100
8120
8140
cz (km s⁻¹)

TABLE 2

PRIMARY ABSORPTION -- SPECTRAL PARAMETERS

Beam	τ_o*	σ† (km s^{-1})
Interferometer	0.27	1.8
Single Antenna	0.14	2.4

* Optical depth at line center.

† Half-width at $\tau = e^{-1/2}\ \tau_o$.

b) Continuum Structure

Amplitudes of the continuum-emission visibility were obtained from the calibrated 4-minute integrations by averaging across the continuum regions of the spectra, excluding both the primary and secondary spectral features (see §IIIa) and the edges of the observed band. The effective continuum bandwidth is about 180 kHz. The resulting data are shown in Figure 3. In their general features these curves agree with the 18-cm NRAO-to-OVRO visibility data of Shaffer and Schilizzi (1975), and with unpublished observations, also at 18 cm, obtained by D. B. Shaffer in 1976 using NRAO, OVRO, and the Onsala Space Observatory at Gothenburg, Sweden.

Models consisting of several elliptical Gaussian components were fitted to the data using a procedure described by Purcell (1973). Since early trials demonstrated the inadequacy of two-component models, several triple models served as initials for this procedure. Three quite different triples, representing different conceptual approaches to reproducing the observed visibility amplitudes, were each developed into a family of more complex models. The addition of new components was frequently suggested by a point-source-grid fitting method due to Pauliny-Toth

Figure 3 - Amplitudes of the interferometer visibility functions. Error bars represent plus and minus one standard deviation. For each interferometer, three model visibility curves are shown, corresponding to three of the models described in the text and shown in Figure 4.

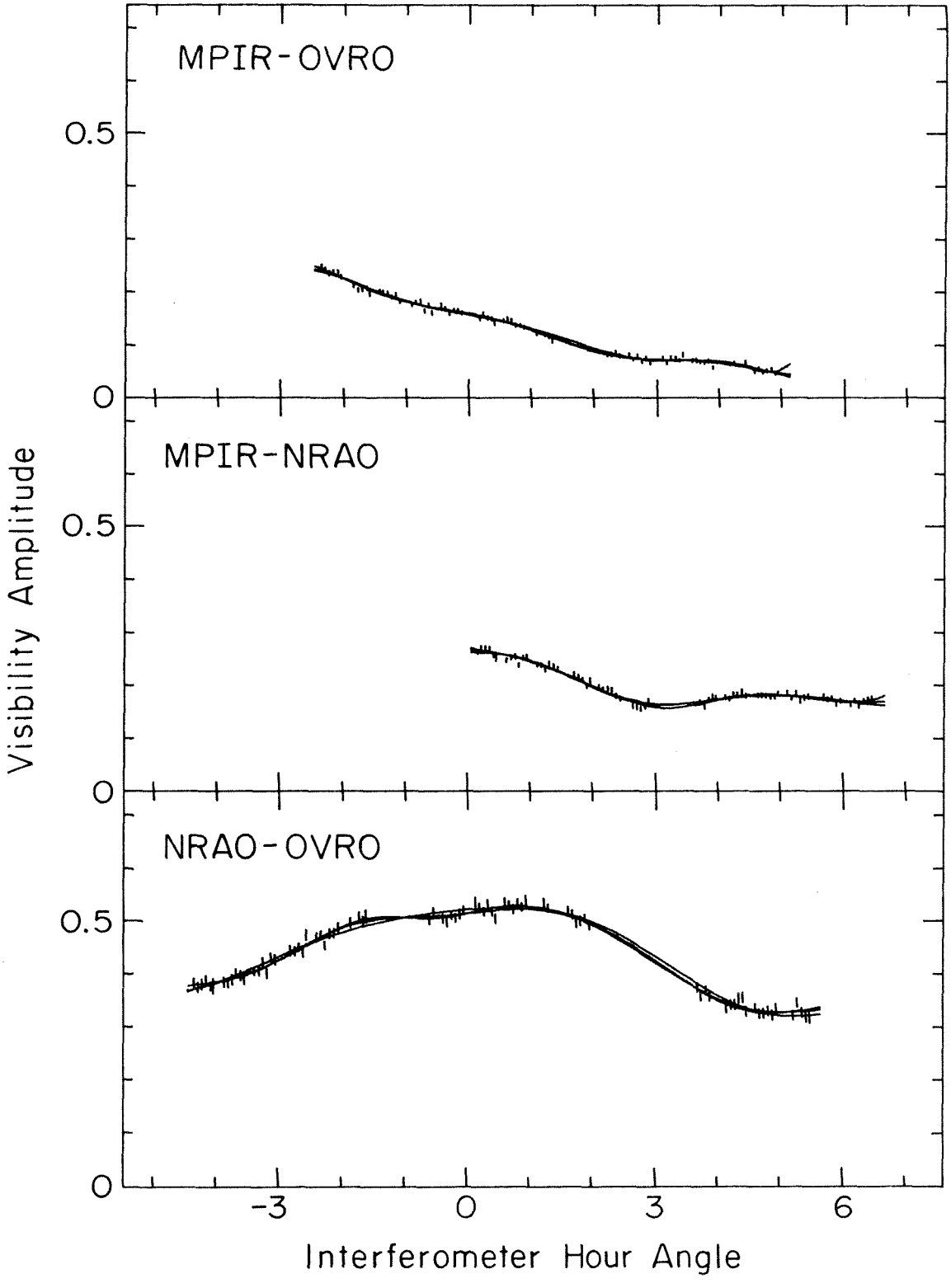
MPIR-OVRO
MPIR-NRAO
NRAO-OVRO
0.5
0
0.5
0
0.5
0
Visibility Amplitude
-3
0
3
6
Interferometer Hour Angle

(Pauliny-Toth et al. 1976).

Eleven final models were developed, each consisting of four or five components, which appears to be the limit of complexity commensurate with the limited (u, v) coverage and apparent simplicity of the visibility function. It must be emphasized that these "components" are a mathematical artifice only, useful for tractably expressing an irregular brightness distribution, but are not physically significant entities. Among these models, the fitting figure-of-merit (the rms of the post-fit residuals, weighted by the individual point errors) ranges from 1.17 to 1.28; since the point errors include no allowance for random error in certain calibration data (see Appendix C), or for systematic errors, these values represent rather good fits.

Figure 4 presents brightness contours of three of the final models convolved with a "clean" interferometer beam. The corresponding visibility amplitude curves are compared with the data in Figure 3.

The models shown demonstrate several general features present in all the final models. A well-determined "nucleus" containing 9.0 Jy (± 0.5 Jy, including the uncertainty in the total flux) is partially resolved at 5 by 8 m arc s (full widths at half power) in position angle -8°. The brightness temperature of this feature reaches

Figure 4 - Brightness contours of three continuum models, and of the clean interferometer beam (lower right panel). The models have been convolved with the beam. Contours represent 5, 10, 15, 20, 30, 50, 70, and 90 percent of the peak brightness in each map. The ticks along the borders are separated by 2 milliarcsec. North is at the top, east at the left.

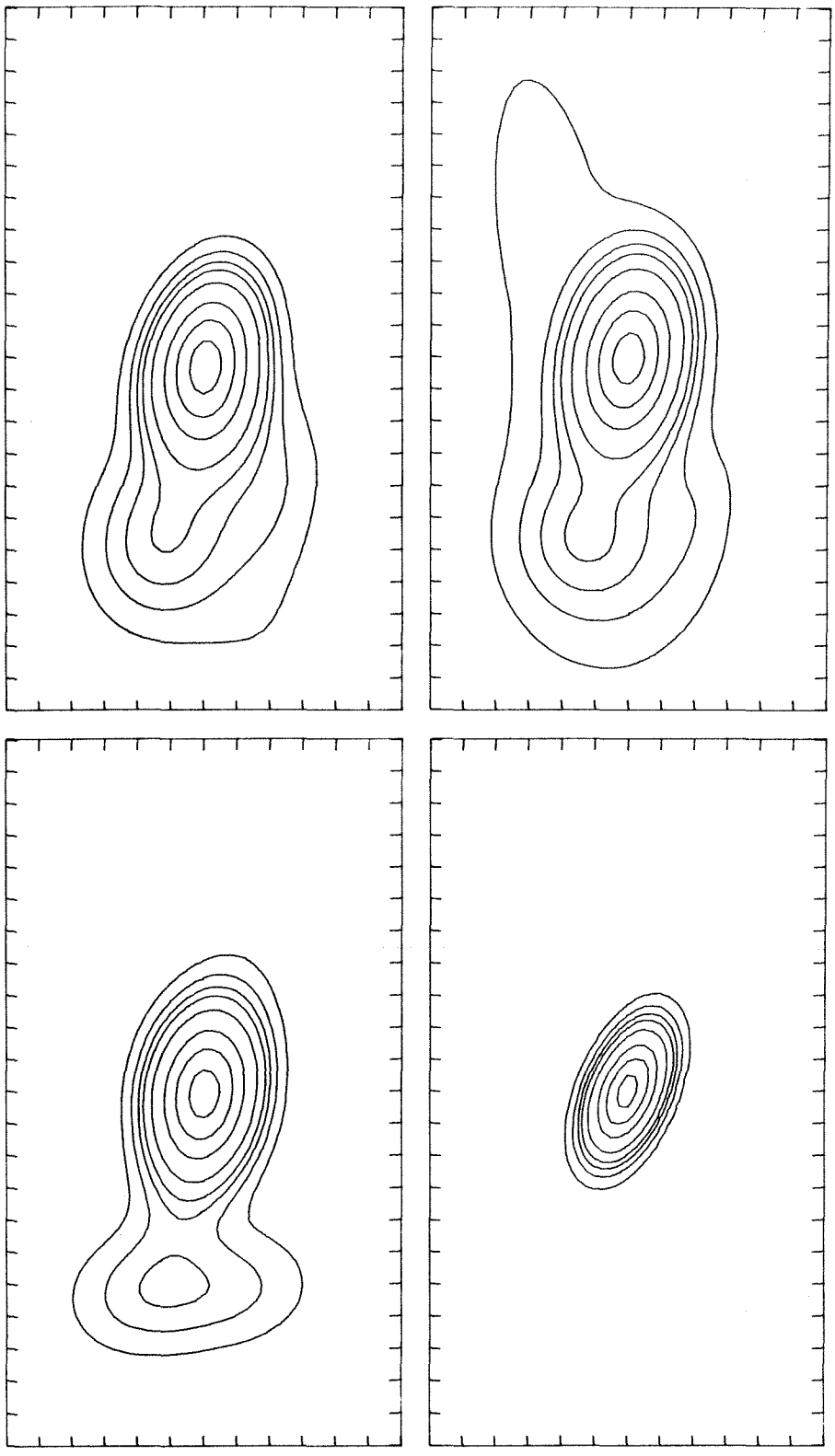

1.5×10^{11} K. A secondary peak or extension, reaching 15 to 20 percent of the main peak's brightness, lies some 12 m arc s away along the direction of the nuclear major axis. These two features are embedded in a weaker "core" extending about 25 m arc s in the north-south direction. Its flux is poorly determined, but in §IVa it is shown to contain about 1.5 Jy. The differences among the models consist primarily in variations in the peripheral structure of this outer region; a narrow structure of low brightness, roughly transverse to the primary orientation, appears in various positions.

In view of the substantial disparity among the initial models, the resemblance among the final models is striking. This "reconvergence" suggests that, within a rather large volume of the multi-parameter model space, only one substantial minimum in the least-square function exists, and that its location can be determined accurately by the present data. Models are not unique, of course, but it appears that if alternative models exist they must be radically different from those presented here. As discussed in §IVa, models of this general form are supported by other observations.

The position angles of models derived from amplitude data alone are subject to an ambiguity of 180°. In Figure 4, and in all references to continuum models hereafter,

this ambiguity is resolved by reference to the closure-phase "hybrid map" which Wilkinson *et al.* (1978) obtained at 609 MHz. Their map is unambiguous in position angle and shows an eccentric core-halo structure, rather larger than those of Figure 4, but clearly extending southwards from the core.

c) Absorption Structure

Relative complex visibility spectra were derived from the long 25-minute integrations by a (complex) normalization with respect to the mean visibility in the continuum. As in the previous subsection, the continuum excluded the spectral features and band edges seen in the mean interferometer spectrum (§IIIa); normalization of the visibility phase included removal of a weak linear slope, determined by fitting in the continuum only. Finally, the three deepest channels in the primary absorption feature, covering the velocity range 8113.0 to 8114.7 km s^{-1}, were averaged to produce the relative line visibility data shown in Figure 5.

Analysis of the absorption structure based on these data proceeded as diagrammed in Figure 6. From a model of the continuum structure, complex continuum visibilities

Figure 5 - Amplitudes (lower part of each panel) and phases (upper part) of the relative line visibility on the three interferometers. Error bars represent plus and minus one standard deviation. Phases are in degrees.

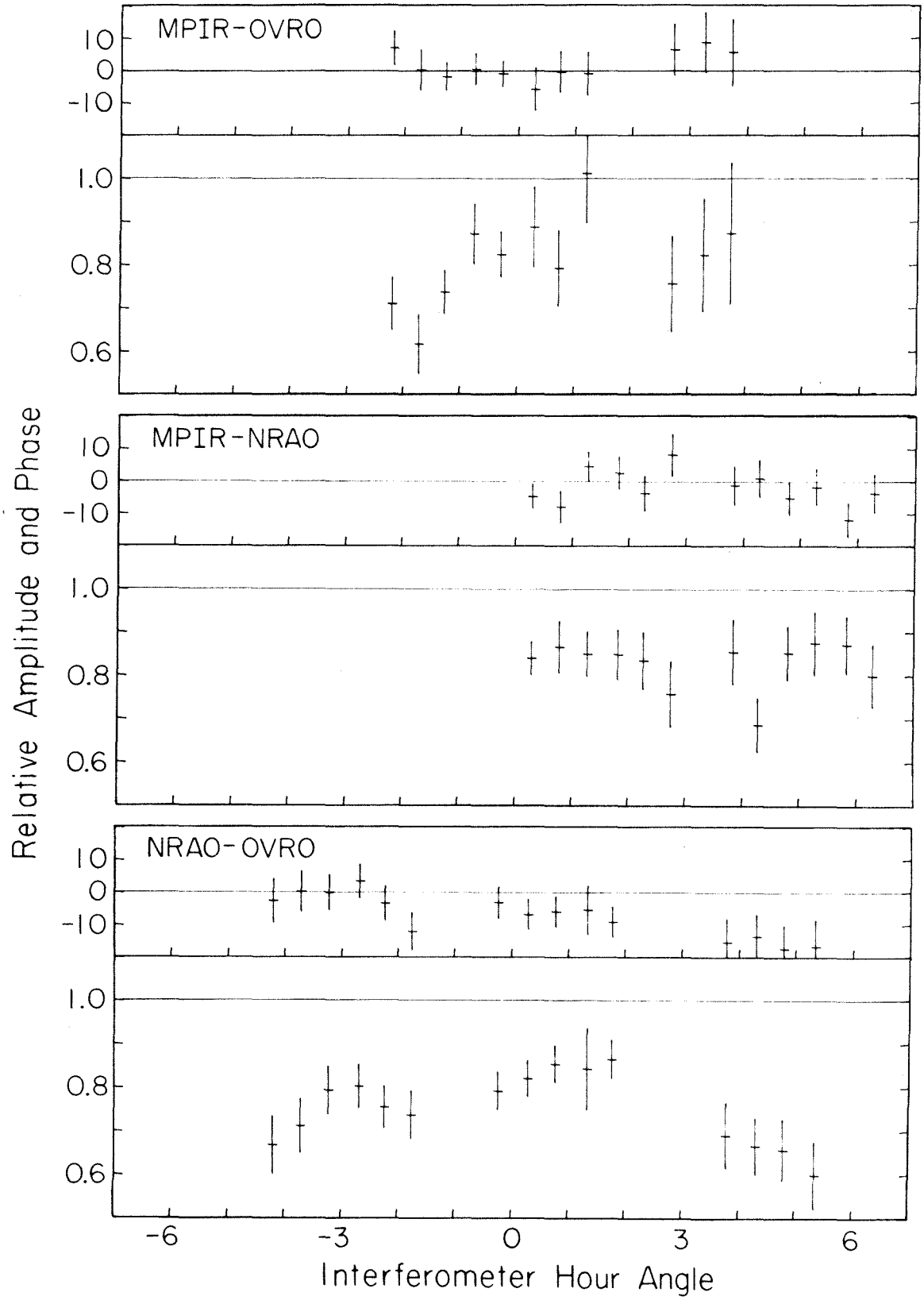
MPIR-OVRO
MPIR-NRAO
NRAO-OVRO
10
0
-10
1.0
0.8
0.6
Relative Amplitude and Phase
-6
-3
0
3
6
Interferometer Hour Angle

Figure 6 - Schematic outline of the absorption mapping procedure. Heavy lines represent primary, light lines auxiliary data; double lines denote complex quantities. Dashed line indicates a comparison to check consistency. Subscript $\underline{o}$ denotes observed quantities; $\underline{c}$ and $\underline{\ell}$ refer to model-dependent continuum and line data. The procedure is described in the text.

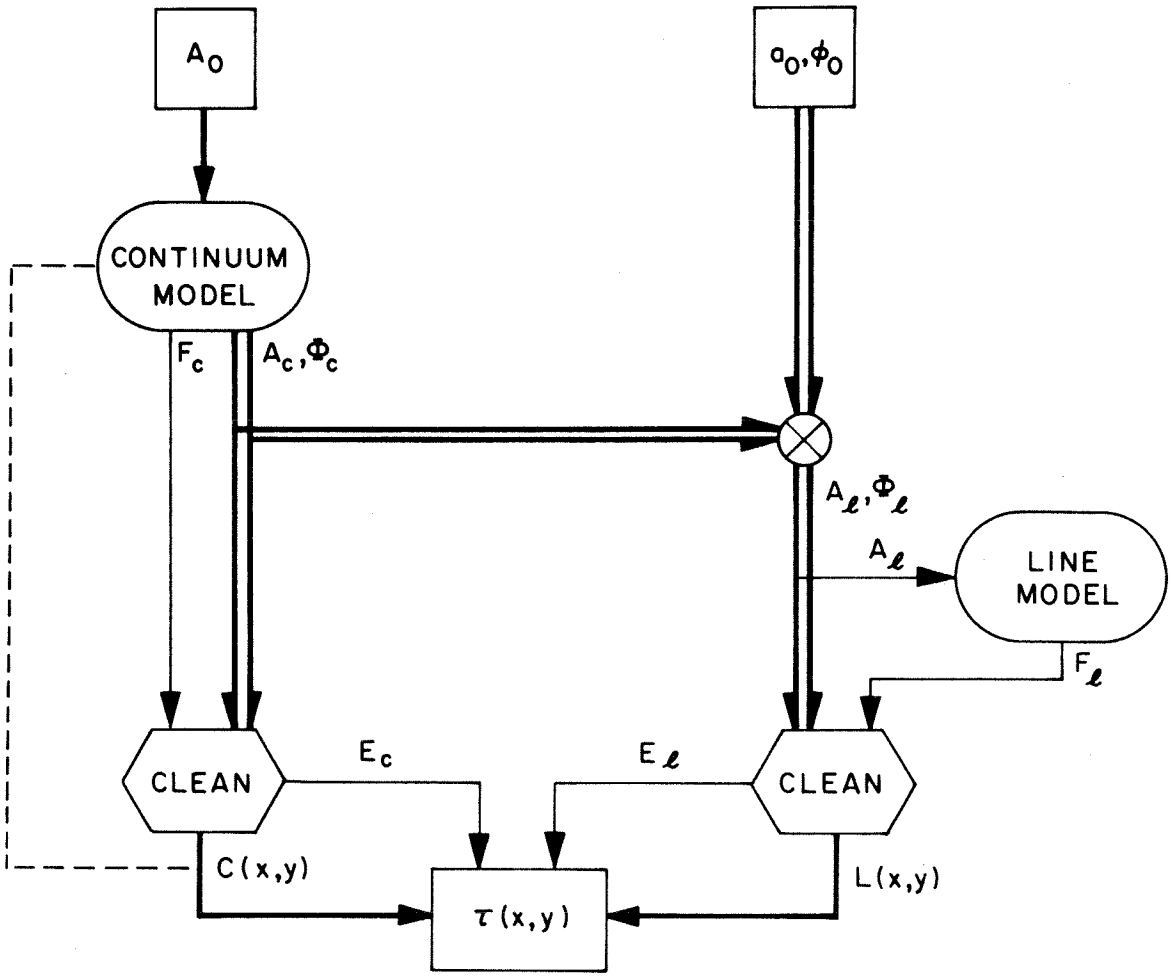
A_0
a_0, ϕ_0
CONTINUUM MODEL
F_c
A_c, Φ_c
A_ℓ, Φ_ℓ
A_ℓ
LINE MODEL
F_ℓ
CLEAN
E_c
E_ℓ
CLEAN
C(x,y)
L(x,y)
$\tau(x,y)$

$A_c \exp(i\Phi_c)$ are calculated. The amplitudes A_c closely match the observed amplitudes A_o, of course; the model is needed only to supply the phase Φ_c. The continuum visibilities are combined with the observed relative line visibilities $a_o \exp(i\phi_o)$ to produce absolute line visibilities $A_\ell \exp(i\Phi_\ell)$. Both the continuum and line visibilities are then reinverted using the CLEAN technique (Högbom 1974), yielding maps $C(x,y)$ in the continuum and $L(x,y)$ in the line. The former should (and does) resemble closely the original model, but is corrupted by residual effects of the "dirty beam" as is the line map, and is thus a more suitable reference for determining the absorption.

Finally, an optical depth map $\tau(x,y)$ is constructed according to

$$\exp [- \tau(x,y)] = L(x,y)/C(x,y). \qquad (2)$$

Optical depths are calculated only where the variance of the ratio $L(x,y)/C(x,y)$ exceeds a fixed value (0.03); this variance is estimated using the residual errors E_c and E_ℓ in the dirty maps after cleaning. (Typically, the rms residual noise is about 0.4% of the peak brightness in the clean map.)

It is evident that the optical depth map is insensitive to any overall scaling errors which might afflict the

observed visibility amplitudes. More important, however, is the corresponding disadvantageous sensitivity to the baseline or zero levels in the continuum and line maps. These levels depend critically upon that bête noire of interferometry, the zero-spacing flux.

Since the zero-spacing flux is the integral of the flux over the entire dirty map, and thus equals the total flux available for the clean map, it can be taken as the total model flux F_c in generating the continuum map. No such recourse is available for the line zero-spacing flux. Single-antenna measurements of the line flux are not satisfactory, because they include the effects of large- and medium-scale components not present in the VLBI continuum model. Instead, a total line flux F_ℓ is derived by fitting a model to the line visibility amplitudes A_l. These fits start from the continuum model, and only the component fluxes are varied.

Results of this analysis are presented in Figure 7, for three cases corresponding to the models shown previously (Figure 4). In all, eight such cases were mapped; all show the same prominent absorption feature displaced to the northeast of the continuum nucleus, and apparently extending northeastward beyond the observable region. Areas of weakly negative optical depth are common in the

Figure 7 - Continuum, line, and optical depth maps (left to right) for the three models shown in Figure 4; each row corresponds to a different model. The border ticks represent 2 milliarcsec, as in Figure 4. The contour levels in the continuum and line maps are as in Figure 4, except that both are scaled to the peak brightness in the continuum map. Optical depth ranges are denoted by hatching, etc., as indicated along the bottom of the figure.

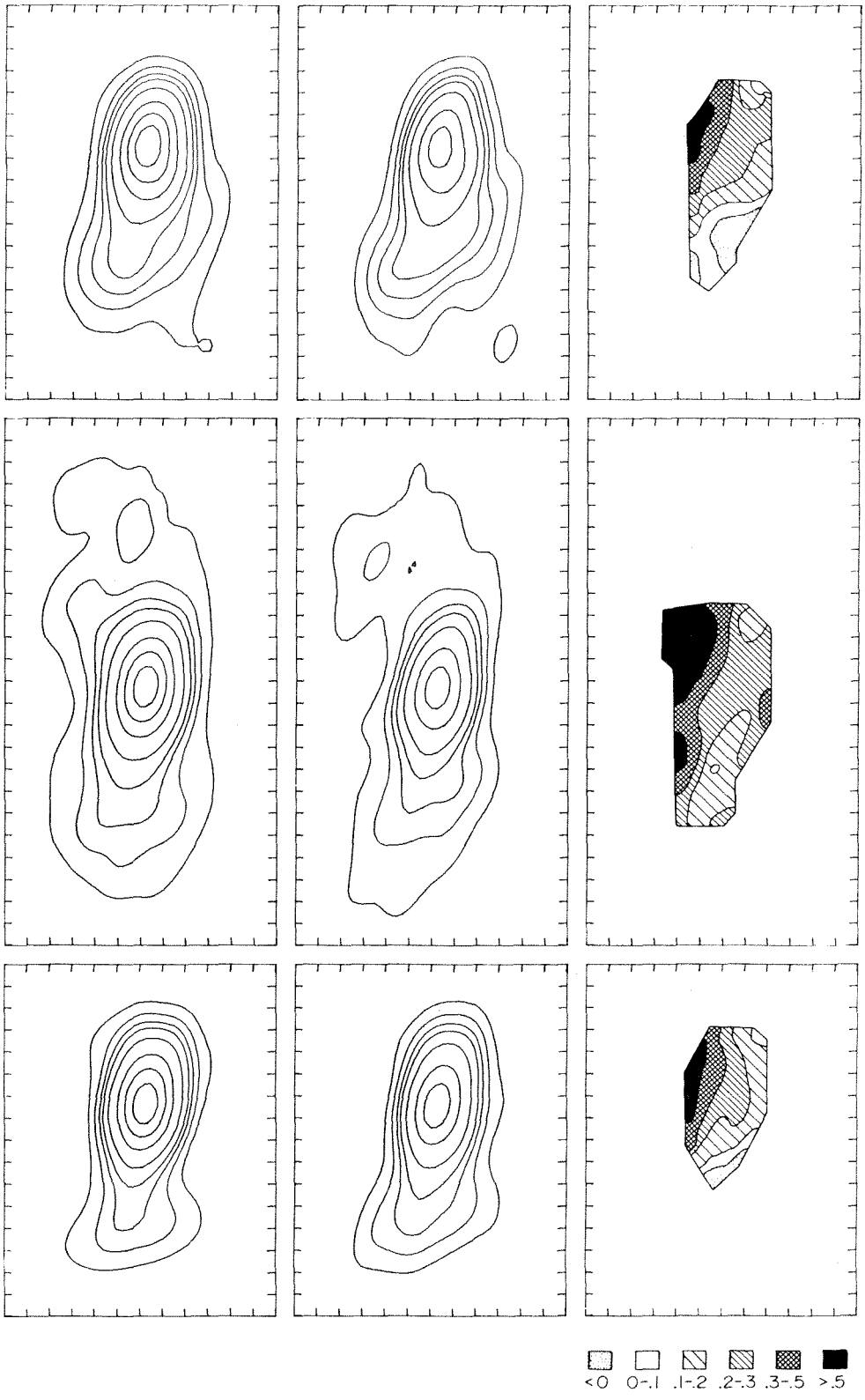
<0
0-.1
.1-.2
.2-.3
.3-.5
>.5

southern or southwestern regions of the maps, suggesting that the zero-spacing fluxes for the line maps were systematically overestimated.

Several tests were performed to check the validity of these maps. The multiplicity of models specifying the continuum brightness serves to test the extent of model dependence in the method of analysis. As discussed in the preceding subsection, these models are thought to delimit the narrow range of variation permissible among the large class of models having this general form. And although they all reproduce the observed continuum visibility amplitudes closely, the phases are unconstrained and vary by as much as 30° among the models. That the observed relative visibility nevertheless determines a similar absorption map in each case argues that this result is not dependent upon the details of the continuum brightness distribution.

Another test excluded the possibility that phase noise significantly affected the derived optical depth map. Several maps were produced with the observed relative phase arbitrarily set to zero; all showed a single prominent absorption feature similar to those in Figure 7, but centered on the continuum nucleus. From this one can conclude that the general shape of the absorption region is

well determined by the relative visibility amplitudes alone, while the phase - particularly along the NRAO-OVRO baseline beyond interferometer transit - is primarily responsible for the positional displacement.

A final test was made to establish that these phase deviations are of astronomical, rather than instrumental, origin. As described in Appendix C, calibration of the phase spectra removes a constant instrumental phase response, determined by observations of pure continuum sources, and assumes that time-dependent instrumental phase effects are negligible. In support of this assumption, the calibration was applied to the individual continuum-source observations, after which relative phases were determined according to the same spectral partition as was used for 3C84. These relative phases are a direct measurement of deviations from the mean spectral response in the critical "line" channels; the measured values and errors are consistent with zero relative phase, and no systematic deviation from zero is discernable.

Table 3 lists basic parameters of the absorption distribution extracted from the full set of optical depth maps. Both the peak optical depth and the angular extent are given as lower limits because the full extent of the absorbing cloud is unknown. The peak optical depth was

estimated by shifting the minimum optical depth of each map to zero before averaging the maxima. This procedure removes at least some of the effect of the systematic error noted earlier in the line zero-spacing fluxes, and also the effects of any accompanying random errors.

TABLE 3

PRIMARY ABSORPTION -- SPATIAL PARAMETERS

Peak Optical Depth	$\gtrsim 0.83$
Angular Extent	$\gtrsim$ 12 m arc s

IV. DISCUSSION

a) Continuum Emission

The present observations, combined with those of Ryle and Windram (1968; hereafter RW) and Miley and Perola (1975; hereafter MP), allow us to describe the 21-cm structure of 3C84 on angular scales covering almost six orders of magnitude. Five distinct components are seen, which we designate as follows:

--The cluster component is an extremely extended emission region covering the center of the Perseus cluster. At 408 MHz, RW see a total of 12 Jy, about 24' by 66' in extent, covering both NGC1275 and NGC1265 (3C83.1), with a faint extension toward IC310. The spectral index of this component is about -0.7, and at 3000 MHz Lynds and Sobieski (1961) detect only a bridge of emission between 3C84 and 3C83.1. Interpolating between these two frequencies and assuming the same extent as seen at 408 MHz, we estimate the brightness of the cluster component at 21 cm to be 2 mJy arcmin^{-2}.

--The halo is roughly coextensive with the filamentary network seen in optical emission lines in NGC1275 and with the diffuse X-ray source (Helmken et al. 1978). The 21-cm synthesis map of MP shows most of the emission (about 1.3 Jy)

concentrated in an elliptical structure with half-power diameters 3!0 by 4!5, oriented generally north-south, which extends asymmetrically northwards (as do the optical filaments). A smaller, weaker concentration lies beyond the filamentary structure, about 3!5 away from NGC1275 in the direction of NGC1272. MP give the flux of the halo as 2.0 Jy at 1415 MHz. This component has a rather steep spectrum (RW find a spectral index of -1.36), and dominates the emission from 3C84 below about 300 MHz.

--The intermediate component was suspected by Wilkinson (1972) and demonstrated by the synthesis observations of MP. It emits 2.2 Jy at 1415 MHz and is elongated, subtending about 12" by 35", in position angle -10°, with a slight asymmetric extension to the south. The spectral index can be estimated from Wilkinson's (1972) suggestion that S(408 Mhz) = 9 Jy, giving an index -1.1. This intermediate component is centered on the nucleus of NGC1275.

--The core refers to the more extended of the milliarcsecond components seen in the present observations. In form it resembles the intermediate component on a scale 1300 times smaller: the half-power diameters are about 9 by 25 m arc s, and the structure is oriented north-south and extends southward from the "nucleus" described next. Both the core and nucleus components are centrally located within the bright optical nucleus of NGC1275. The flux of the core

could not be determined accurately from the present observations, but if we adopt MP's values for the halo and intermediate component fluxes (total 4.2 Jy) and the nucleus flux (9.0 Jy) determined from the models in §IIIb, then the core must radiate about 1.5 Jy to make up the total of 14.7 Jy observed. (In this calculation we have ignored the small effects due to the cluster emission and the spectral slopes between 1415 and 1383 MHz.)

--The variable nucleus, finally, emits most of the flux of 3C84 at this frequency. At the epoch (1975.93) of the present observations it radiated 9.0 Jy from an elliptical region with half-power diameters 5 by 8 m arc s, in position angle -8°, and reached a peak brightness temperature of 1.5×10^{11} K.

High-resolution observations at this epoch near 21 cm offer a unique opportunity to study the core and nucleus components simultaneously, for only in this region of the spectrum are their fluxes currently comparable. This can be seen clearly by reference to the spectral decomposition of Pauliny-Toth et al. (1976) or Kellermann et al. (1971). The core is the "decimeter" component suggested by Kellermann et al. (1971) from rudimentary VLBI observations at 18 cm, and mapped at 49 cm by Wilkinson et al. (1978). At 21 cm the core is optically thin with a rather steep spectral slope.

The nucleus, on the other hand, is optically thick at 21 cm and contains the very complex milliarcsecond structure which has been studied extensively at high frequencies (Niell et al. 1975; Legg et al. 1973; Schilizzi et al. 1975; Pauliny-Toth et al. 1976; Wittels et al. 1975). None of this fine-scale structure is visible in the 21 cm results; from the model-fitting described in §IIIb we can set an upper limit of about 0.3 Jy on the flux of components a milliarcsecond or less in diameter.

The observed ratio of the core and nucleus fluxes does not agree well with the spectral decomposition of Pauliny-Toth et al. (1976) for epoch 1974.5, which suggests almost equal fluxes. However, the flux of the nucleus has increased by $\sim$ 2 Jy since that epoch (we derive 7.1 Jy in 1974.6 by subtracting the core flux from the total compact flux of 8.6 Jy reported by Ekers, van der Hulst, and Miley [1976]). The decomposition by Pauliny-Toth et al. (1976) assumes that the core has not varied since 1969; however, if the flux values given by MP are correct then some component has decreased in flux between 1968.0 (Kellerman and Pauliny-Toth 1968) and 1971.4, before the onset of the currently observed sharp increase. Such variations are consistent with the (minor) diameters of either the core

(14 light years) or the nucleus (8 light years).[1]

The simultaneous observation of the core and nucleus components allows us to confirm what has long been presumed, that these two regions are concentric. Through the results of RW and MP we can extend this concentricity to the entire hierarchy of radio structure. Throughout this hierarchy, except for the cluster component, we also observe the pervasive geometrical alignment in position angle $\sim 10°$ which has often been remarked (MP; Pauliny-Toth et al. 1976).

---

[1]Throughout this paper the linear scale at NGC1275 corresponds to a distance of 95.9 Mpc, based on $z = 0.0176$ and $H_o = 55$ km s^{-1} Mpc^{-1}.

b) Absorption

In the primary absorption line, the column density of atomic hydrogen in the direction of the peak observed optical thickness is $N_H = (6.7 \times 10^{18})\ T_s\ cm^{-2}$, where we have assumed a Doppler-broadened line profile, with width equal to that observed in the interferometer spectrum (Table 2). The spin temperature T_s, assumed uniform throughout the absorbing region, cannot be determined observationally, but we can set a fairly stringent limit by assuming the hyperfine atomic states to be in thermal equilibrium at the gas kinetic temperature T_k. If the entire line width seen by the interferometer (Table 2) is due to thermal Doppler broadening then $T_s = T_k \simeq 400$ K; and since the narrowing of the line with increasing angular resolution is suggestive of turbulent broadening, we can assume $T_s < 400$ K.

Theoretical and observational results pertaining to galactic HI regions may also be relevant to estimating the kinetic temperature in the present case. Calculations of the equilibrium between heating by cosmic rays, X-rays, and ultraviolet radiation, and cooling by bremstrahlung and metallic and molecular line radiation, indicate that quite low temperatures $T_k = 20$ to 70 K may prevail in dense

regions (Kaplan and Pikel'ner 1974; Dalgarno and McCray 1972; Field 1971). Absorption by galactic hydrogen against extragalactic sources indicates a wider range, from 20 to 200 K (Greisen 1973a; Radhakrishnan et al. 1972a, 1972b; Radhakrishnan and Goss 1972; Hughes, Thompson, and Colvin 1971). There are also both theoretical and observational indications of a high-temperature, low-density phase in the interstellar medium, but its temperature is well above the present 400 K limit.

In Table 4 we present deduced parameters of the absorbing cloud, for three plausible values of the spin temperature. The column density given is a lower limit, since we may not be seeing the thickest part of the cloud. The mean density n_{HI} and total mass M_{HI} are calculated assuming a spherical volume with diameter equal to the observed linear extent of 5.6 pc.

Field (1958) has shown that under certain conditions radiative absorption from an intense 21-cm continuum may dominate collisional de-excitation, drawing the spin temperature upwards towards the characteristic radiation temperature

$$T_r = \frac{\lambda^2}{2k} \bar{I} = \frac{\Omega}{4\pi} T_b \quad , \tag{3}$$

where $\bar{I}$ is the mean specific intensity, here assumed to emanate from a source with brightness temperature T_b subtending solid angle Ω. The last two entries in Table 4

TABLE 4

CLOUD PARAMETERS

	T_s or T_k (K)		
	30	100	300
N_{HI} (cm^{-2})	2.0×10^{20}	6.7×10^{20}	2.0×10^{21}
n_{HI} (cm^{-3})	12	39	116
M_{HI} ($M_\odot$)	26	88	266
τ_r (10^6 y)	17	9.3	5.4
τ_k (10^6 y)	22.8	24.6	44.2

show that such an effect is unlikely to prevail in the present case, justifying the earlier assumption that $T_s = T_k$. The "absorption timescale" τ_r is the interval during which T_r exceeds the tabulated T_s for gas moving radially with respect to the main body of NGC1275 at the observed velocity of 3000 km s^{-1}. In calculating τ_r only the contribution from the radio nucleus, which dominates all the other components at any distance, has been used.

The "thermalization timescale" τ_k is the characteristic time for collisional de-excitation to bring T_k into equilibrium with T_s, assuming initially $T_k << T_s$. Field (1958) treats T_k as fixed and ignores this process, presumably because it is slow compared with radiative absorption when $T_k >> T_s$. In the present case, however, it is important to know how long T_k will remain below the observed limits. Using Field's notation, we write the energy flow from the hyperfine atomic states into the gas as

$$\frac{d}{dt}\ (kT_k) = kT_* \frac{n_1 P_{10} - n_0 P_{01}}{n_0 + n_1} \qquad (4)$$

where $T_* = h\nu_{10}/k = 0.0681$ K. The populations n_0 and n_1 of the atomic states are determined by a Boltzmann distribution at temperature T_s, and the collisional excitation and de-excitation rates P_{01} and P_{10} are related by a similar relation at temperature T_k. Thus

$$\frac{d}{dt}\ (kT_k) \ = \ \frac{3}{4}\ kT_* \ \left(\frac{T_*}{T_k} - \frac{T_*}{T_s} \right) \ P_{10} \quad , \quad (5)$$

where we have assumed $T_k >> T_*$ and $T_s >> T_*$. Taking $T_s >> T_k$, we derive the characteristic time

$$\tau_k \ = \ \frac{kT_k}{\frac{d}{dt}\ (kT_k)} \ = \ \frac{4}{3}\ (T_k/T_*)^2\ P_{10}^{-1} \quad . \quad (6)$$

The entries in Table 4 were calculated using the rate coefficients of Allison and Dalgarno (1969) for spin-exchange collisions among hydrogen atoms (the dominant effect in regions as dense as those contemplated here).

From the tabulated timescales we conclude that thermal population of the spin states must prevail except during the few tens of millions of years just before collision, if the absorbing cloud is falling into the main body of NGC1275. And if the cloud has been ejected, equilibrium should be established within about fifty million years after ejection. This amply justifies our neglect of possible emission in equation (2).

We comment finally on the weaker of the two secondary spectral features. It is clearly seen at 8107 km s^{-1} in the single-antenna spectrum (Fig. 2), but has vanished into the noise in the interferometer spectrum. The cloud causing this feature must be seen against the more extended core region only; at high resolution the background is sufficiently weakened that the absorption feature is no

longer detectable. (Similarly, the stronger secondary feature at 8120 km s^{-1} must be more centrally positioned with respect to the continuum nucleus than the deep primary feature, since its relative strength increases in the interferometer spectrum.) The alternative hypothesis that the 8107 km s^{-1} feature is due to heavy absorption against the intermediate component is untenable; this would require a large cloud covering at least 15 percent of the intermediate component and thus subtending about 8", which cannot be reconciled with the narrow velocity range seen.

c) Interpretation

The observations reported here augment the already extensive observational literature on NGC1275. The discovery of the 21-cm absorption line by DeYoung, Roberts, and Saslaw (1973; hereafter DRS) and the synthesis study by Ekers, van der Hulst, and Miley (1976; hereafter EHM) have already been mentioned (§I), as have the observations of the structure and spectrum in the radio continuum (§IVa). Optically, the recent papers by Rubin, Ford, Peterson, and Oort (1977; hereafter RFPO) and Rubin, Ford, Peterson, and Lynds (1978; hereafter RFPL) have provided a wealth of spectroscopic data and, in particular, a comprehensive mapping of the velocity fields at both high and low

velocities. Also germane are the absolute spectral measurements by Shields and Oke (1975) and Wampler (1971). Adams (1977) has published visible ultraviolet and near infrared plates, and the extensive studies of NGC1275 and the Perseus Cluster in X-rays include both structural (Helmken et al. 1978; Wolff, Mitchell, Charles, and Culhane 1976) and spectral (Serlemitsos et al. 1977) observations.

Two hypotheses, neither completely satisfactory, have been advanced to elucidate the high-velocity features in NGC1275. We outlined the historical development of these models in §I; here we describe them more thoroughly with reference to recent observational results, and discuss the significance of the present observations to each. Finally, we comment on the objections which have been raised against both models.

In the superposition hypothesis the two velocity systems arise in distinct galaxies which we see superposed along the line of sight. We ignore the case in which the galaxies are colliding, as there seems to be no evidence for collision (Adams 1976; van den Bergh 1977).

The low-velocity spectrum is associated with the background galaxy, an elliptical or S0 system with an extremely compact central source of optical (RFPO), radio (§IVa), and possibly X-ray (Helmken et al. 1978) emission. The region

near the nucleus has experienced recent star formation (Oort 91976; van den Bergh 1972; Minkowski 1968). Surrounding this galaxy are the network of emission-line filaments and the intermediate and halo radio components; the filaments show no coherent velocity pattern (RFPL). The background galaxy, with its extended features, is approximately at rest with respect to the core of the Perseus Cluster.

The foreground galaxy, which is falling towards the cluster core at $\sim$ 3000 km s^{-1}, is responsible for the high-velocity features. As delineated by the optical emission lines (RFPL), it lies to the north and west of the nucleus in position angles ranging from -90° to +60°, with a maximum extent of some 28 kpc (taking the distance to be the same as that of the background galaxy) along a roughly east-west axis. The galaxy is of late spiral (RFPO) or perhaps Magellanic (Oort 1976) type, rotating with a maximum velocity of 150/sin i km s^{-1}, and seen nearly edge-on (RFPO). The optical and ultraviolet emission is dominated by the intense blue knots, which appear to be high-excitation, metal-poor HII regions (RFPO; Shields and Oke 1975; Burbidge and Burbidge 1965; Adams 1977); closely associated with the emission regions are prominent absorption lanes which obscure the stellar continuum from the background galaxy (RFPO; Oort 1976). The absorption knots

also redden the emission of the background nucleus (van den Bergh 1977; Shields and Oke 1975; Wampler 1971) and steepen the Balmer decrement in the low-velocity emission lines from the background filaments (RFPO). There is sufficient obscuration in the foreground galaxy that its own stellar absorption spectra cannot be seen against the brighter background (RFPO; Oort 1976), and the nucleus of the foreground system either is similarly obscured or is absent, although infrared observations might reveal its presence (RFPO). The 21-cm absorption, finally, arises in an "interstellar" HI cloud within the foreground galaxy, which lies directly along our line of sight to the bright background nucleus; this requires that the HI extend somewhat beyond the visible optical emission region (which RFPO assert does not extend into the nucleus).

The superposition hypothesis receives strong support from the results of §III. The absorption is indeed concentrated in front of the two very compact components of continuum emission, as is required by the hypothesis. Agreement between the radio absorption velocity of 8114 km s^{-1} and the optical emission velocities is difficult to assess. RFPL (in particular Fig. 4a) were only able to determine velocities to within 5" of the nucleus; these values cluster somewhat above 8200 km s^{-1}, but lie on an abruptly flattened part of the velocity curve. Extrapolat-

ing these closest points to the nucleus gives 8190 km s^{-1}, while extrapolation from points 10" to 20" from the nucleus yields 8030 km s^{-1}. Within this rather large uncertainty the radio absorption velocity supports the prediction of the superposition hypothesis. It has been suggested (S. M. Kent, private communication) that interstellar absorption lines might be observable against the bright nucleus. Such lines should be very close to the 21-cm velocity of 8114 km s^{-1}.

Further, the deduced physical parameters of the absorbing cloud (Tables 2, 3 and 4) are gratifyingly similar to those observed in cold galactic HI clouds. The line width, peak optical depth, and column density agree closely with those reported by Radhakrishnan et al. (1972a, 1972b) and Radhakrishnan and Goss (1972). Assuming $T_s \lesssim 60$ K as found by these authors for optically thick clouds, the density deduced here is somewhat lower than the 100 cm^{-3} which Greisen (1973a, 1973b, 1973c) suggests is typical. The linear scale of the absorption seen in NGC1275 is very close to the typical value of 5 pc which Baker and Burton (1975) derive from synthetic-profile two-phase modelling of the interstellar medium based on emission-line observations; absorption structures as small as those suggested by Greisen (1973a, 1973b, 1973c) would not be resolved by the present observations. Following van den Bergh (1977), we

can calculate the hydrogen column density from the observed reddening $E_{B-V} = 0.44$, using the galactic gas-to-dust ratio (Knapp and Kerr 1974); we find $N_{HI} = 2.2 \times 10^{21}$ cm^{-2}, which agrees with the present result for $T_s = 300$ K. Finally, the derived densities are consistent with theoretical models of the interstellar medium, which suggest $n_{HI} = 20$ to 100 cm^{-3}, with T = 20 to 70 K (Kaplan and Pikel'ner 1974; Dalgarno and McCray 1972; Field 1971). While physical conditions in the putative foreground galaxy can be expected to differ from those in the galactic interstellar medium, the present results clearly suggest absorption by an interstellar cloud in an intervening spiral galaxy.

Such a galaxy would contain many clouds like the one contemplated here. The question arises whether these clouds would be detectable in absorption against the intermediate continuum component (§IVa). The small size of the clouds would present structure visible to the VLB interferometer beam used here, but the effective brightness of even an opaque cloud would be only that of the intermediate component, fainter than the nucleus by a factor of forty million and far below the sensitivity limit of the interferometer. Most clouds would also be outside the interferometer's fringe rate "window".

Single-antenna observations will not reveal the clouds either. The high-velocity gas mapped by RFPL can obscure no more than 1 Jy of the intermediate-component flux, even if totally opaque, resulting in $\tau \lesssim 0.07$ as seen by the antenna beam. And this absorption would be spread out over $\sim$ 150 km s^{-1} (8085 to 8286 km s^{-1} in RFPL's velocity map), producing a very weak, wide feature extending beyond the observed band. Similar considerations apply to observations with the Westerbork Synthesis Radio Telescope (cf. EHM), whose synthesized beam covers about 40 $arcsec^2$ and would include a large number of clouds. Subtraction of the unresolved core and nucleus components might allow such a broad feature to be observed; the velocity gradient seen by RFPO should then be discernable.

Objections to the superposition hypothesis have been reviewed recently by van den Bergh (1977). The most cogent objections concern the morphology of the assumed foreground galaxy. The absence of a nucleus (Oort 1976) or stellar continuum (Burbidge, Smith, and Burbidge 1978), and the abundance of emission regions and obscuring matter (RFPO) without evidence of coherent spiral structure, all suggest a very late spiral or irregular galaxy. On the other hand, the diameter of this galaxy (28 kpc) is incompatible with such a classification. This difficulty is exacerbated if, as van den Bergh (1977) suggests, the bright blue knots to

the southeast of the nucleus do indeed belong to the high-velocity system, bringing its diameter to 60 kpc. Radial velocities have not been measured for these features, but Adams (1977) points out that they are bright in the ultraviolet, as are the identified high-velocity knots, and appear to be connected to the main body by a bridge of ultraviolet emission.

Further, as emphasized by Oort (1976) and van den Bergh (1977), such galaxies seldom occur in the cores of rich clusters. Controverting this point, RFPO note the presence of a similar galaxy 3!5 northeast of NGC1275. The superposition hypothesis does not require that the foreground galaxy be in the core, although of course the probability of superposition is greater in that case. We note in this connection that the high relative velocity implies both that the foreground galaxy is at least near the cluster core, and that it has been in the outer regions of the cluster throughout most of its existence.

A number of the arguments raised against the superposition hypothesis appear to be cases of Occam's Razor. As van den Bergh (1977) notes, the unusual features of the presumed background galaxy must separately be accounted for: the Seyfert nucleus and radio and X-ray emission, the presence of young stars, and the low-velocity emission filaments. Of these, the most compelling point concerns

the filaments, which, following Burbidge and Burbidge (1965), have frequently been attributed to an explosive event in the nucleus of NGC1275 (van den Bergh 1977; Adams 1977; Oort 1976). Kent (1978), however, proposes that the filaments are condensations of intra-cluster gas which have accreted and cooled in the potential well of NGC1275 and the cluster core.

Also in this vein, Burbidge, Smith, and Burbidge (1978) have reported the presence of high-velocity optical emission lines in the radio galaxy DA240. Here the high-velocity lines are blue-shifted with respect to the galaxy, and show a shallow velocity gradient of $\sim$ 50 km s^{-1} over 14 kpc. Since DA240 is not in a cluster, an interpretation based on superposed galaxies is untenable here. The degree to which this casts doubt upon the superposition hypothesis for NGC1275 depends on the extent of similarity between the two cases; this does not seem to have been established yet.

The preceding arguments illustrate the attractive feature of the ejection hypothesis, which subsumes all the observed features of NGC1275, including the presence of two velocity systems, under a single explanation involving the active nucleus. A single galaxy, much like the elliptical background galaxy described above for the superposition hypothesis, forms the main body. The nucleus of this

galaxy, containing the very compact optical (RFPO), radio (§IVa) and possible X-ray components (Helmken et al. 1978), has experienced a major explosion (Burbidge and Burbidge 1965) which ejected the material forming the low-velocity filaments; this material has since come approximately to rest (RFPL). The explosion has induced a burst of star formation (Oort 1976; van den Bergh 1972; Minkowski 1968).

A second ejection process, acting continuously, and at a constant velocity, over a period of $\sim 7 \times 10^6$ years, has produced the high-velocity features (Burbidge and Burbidge 1965), which are now behind the main body. The ejection is driven by a galactic wind or line-locking mechanism (DRS), and is confined to a sector of a cone, with axis almost parallel to our line of sight (cf. positions and velocities of RFPL). The low-density matter ejected is photoionized by the Seyfert nucleus (Shields and Oke 1975), forming the emission knots, while a few denser clumps remain neutral and are seen in 21-cm absorption against a radio component larger than the nucleus (DRS). The background component may be concentric with the nucleus, the regions more distant than the ejected neutral gas forming the background. Or, the larger component may be separate from the nucleus and behind it along our line of sight.

The present observations appear to contradict one of the fundamental predictions of the ejection hypothesis. As

is clear from the optical-depth maps of Figure 7, substantial absorption is seen in front of the continuum nucleus; the absorbing gas thus cannot have been ejected from the nucleus. Further evidence is provided by the shape of the absorbing region, which is noticeably convex towards the nucleus. Were the nucleus in the foreground, we would observe a concave or annular conformation.

Further, we can exclude the case in which the absorbing hydrogen is still within a concentric component forming the background continuum. This component could only be the optically-thin core (§IVa), but its flux is insufficient to produce the observed line. And the dimensions of the core restrict the duration of such a condition to less than two thousand years. Hence the background component must lie at some distance behind the nucleus, closely aligned along the line of sight. The ejection model is thus on an equal footing with the superposition hypothesis in requiring a positional coincidence.

Other observational results have also called the ejection hypothesis into question. RFPO and Oort (1976) have argued convincingly that obscuring matter is seen in front of the main body of NGC1275, and that the high-velocity emission knots are closely associated with this obscuration. And Adams (1977) has pointed out that his ultraviolet plates give evidence of hot stars in the high-

velocity knots, which is unlikely if the high-velocity matter is to be ejected continuously. The existence of such late-type features and the reddening of the elliptical component are in any case inexplicable without extensive embellishment of the ejection hypothesis.

V. SUMMARY

Most of the 21-cm flux of 3C84 is concentrated in an extremely compact variable component in the nucleus of NGC1275. This optically-thick "nucleus" contains the complex milliarcsecond structure seen at higher frequencies; at 21 cm only a smooth elliptical distribution is seen, with half-power diameters 5 by 8 m arc s, in the same position angle as previously-known structures four orders of magnitude larger. At epoch 1975.93, the nucleus radiated 9.0 Jy, corresponding to a brightness temperature of 1.5×10^{11} K. The optically-thin "core" component prominent at decimeter wavelengths is also seen, and is roughly concentric with the nucleus.

The primary 21-cm absorption feature in NGC1275 arises in an HI cloud covering part of the intense, compact continuum nucleus. Although absorption is seen against the brightest part of the continuum structure, the cloud is displaced to the northeast from the nucleus, reaching optical depths of at least 0.83. A lower limit to the size of the cloud is 5.6 pc, the extent of the region in which absorption is detectable. Assuming a spherical cloud with this diameter and a spin temperature of 100 K, we deduce a volume density of 39 cm^{-3}. The weaker 21-cm features also

absorb against the two compact continuum structures.

The observed disposition of the absorbing cloud, and the similarity of the derived physical parameters to those believed to prevail in galactic HI clouds, strongly support the interpretation that all the high-velocity features arise in a superposed galaxy in the Perseus Cluster; the line of sight to the high-brightness continuum source in the nucleus of the background galaxy picks out the particular cloud in the foreground galaxy in which the absorption occurs.

In contrast, the presence of absorption in front of the active nucleus is inconsistent with the alternative interpretation in which the high-velocity gas is ejected from the nucleus.

A formidable body of observations now firmly substantiates a superposed-galaxy interpretation of the high-velocity features. While this picture requires a rather peculiar foreground galaxy and does not explain the active nucleus and filamentary structure in the background galaxy, it no longer appears possible to construct a unified model based on ejection of the high-velocity features from the nucleus.

APPENDIX A - ASYMMETRIC CLIPPING

The "clippers" which effect the one-bit digitization in the Mark II VLBI recording system do not, in general, change states at exactly zero voltage. This appendix derives the resulting distortion of the one-bit autocorrelation function. (A similar distortion is eliminated from the crosscorrelation function by the "fringe rotation" in the VLBI processor.)

We consider a covariance-stationary normal stochastic process, $X(t)$, with zero mean, unit variance, and covariance function $r_X(\tau)$; $r_X(\tau)$ is the true autocorrelation function in VLBI parlance. This process is the input to an asymmetric clipper, whose output is another stationary normal process,

$$Y = f(X) = \begin{cases} -b, & X < a-b, \\ X-a, & a-b \leq X \leq a+b, \\ b, & X > a+b, \end{cases} \qquad \text{(A1)}$$

where a is the transition level and 2b is the width of the transition region. We assume $b^2 << a^2 << 1$. The observed autocorrelation function is then $r_Y(\tau)$, the covariance

function of the output process Y(t), given by

$$R \equiv r_Y(\tau) = \int_{-\infty}^{\infty} du \int_{-\infty}^{\infty} dv\, f(u)f(v)\, \frac{\exp[-(u^2+v^2-2uvr)/2(1-r^2)]}{2\pi\sqrt{(1-r^2)}}, \quad (A2)$$

where $r \equiv r_X(\tau)$.

Middleton (1946) has analyzed a similar but rather more complex problem. While equation (A11) below can be obtained as a particular case of his results, a much more straightforward derivation, outlined below, is possible in this restricted case.

Following Van Vleck and Middleton (1966) - who treat the case of vanishing a and arbitrary b in equation (A1) - we represent the clipping function as a contour integral;

$$f(x) = \frac{1}{2\pi} \int_{C^-} e^{i(x-a)z}\, \frac{e^{-ibz}-1}{z^2}\, dz - \frac{1}{2\pi} \int_{C^+} e^{i(x-a)z}\, \frac{e^{+ibz}-1}{z^2}\, dz, \quad (A3)$$

where the contours C^+ and C^- extend along the real axis from $-\infty$ to ∞ except for indentations around the origin in the direction of $\pm$ i. This representation may easily be verified using the residue theorem by closing the contours with a semicircle of infinite radius in either the positive- or negative-imaginary half plane, such that the real exponent is negative.

We substitute equation (A3) into equation (A2), and interchange the order of integration; the integrals over u and v perform a two-dimensional Fourier transform of the joint normal probability density, with the result

$$R = \frac{1}{4\pi^2}\left[\int_{C^-} dz \int_{C^-} dz'\ (e^{-ibz}-1)(e^{-ibz'}-1)\ F(z,z') - \int_{C^-} dz \int_{C^+} dz'\ (e^{-ibz}-1)(e^{+ibz'}-1)\ F(z,z') - \int_{C^+} dz \int_{C^-} dz'\ (e^{+ibz}-1)(e^{-ibz'}-1)\ F(z,z') + \int_{C^+} dz \int_{C^+} dz'\ (e^{+ibz}-1)(e^{+ibz'}-1)\ F(z,z')\right], \quad \text{(A4)}$$

where $$F(z,z') = \frac{e^{-iaz}}{z^2}\ \frac{e^{-iaz'}}{z'^2}\ e^{-(z^2 + z'^2 + 2zz'r)/2}. \quad \text{(A5)}$$

The simple r-dependence in this formulation facilitates expansion of R in a Taylor series. It will prove advantageous to separate the even- and odd-order terms:

$$R = \sum_{k=o}^{\infty} (C_{2k}\ r^{2k} + C_{2k+1}\ r^{2k+1}), \quad \text{(A6)}$$

where

$$C_{2k} = \frac{1}{\pi^2 (2k)!}\left[\int_{-\infty}^{\infty} \sin ax\ \sin bx\ x^{2k-2} e^{-x^2/2}\ dx\right]^2, \quad \text{(A7)}$$

and

$$C_{2k+1} = \frac{1}{\pi^2 (2k+1)!} \left[\int_{-\infty}^{\infty} \cos ax \sin bx \, x^{2k-1} \, e^{-x^2/2} \, dx \right]^2 . \quad \text{(A8)}$$

The contours C^+ and C^- have both been reduced to the real axis because the integrands are analytic for $k \geq 0$.

Since we assume a and b are small, and the Gaussian factor restricts the integrands to moderate values of x, we expand the trigonometric functions in power series and integrate term by term. Keeping only the first-order term in b and terms through second order in a,

$$C_{2k} = \frac{2}{\pi} \frac{[ab(2k-1)!! - \ldots]^2}{(2k)!}$$

$$\cong \frac{2}{\pi} a^2 b^2 \frac{(2k-1)!!}{(2k)!!} , \quad \text{(A9)}$$

and

$$C_{2k+1} = \frac{2}{\pi} \frac{[b(2k-1)!! - 1/2 \, a^2 b(2k+1)!! \ldots]^2}{(2k+1)!}$$

$$\cong \frac{2}{\pi} b^2 \frac{(2k-1)!!}{(2k+1)(2k)!!} - \frac{2}{\pi} a^2 b^2 \frac{(2k-1)!!}{(2k)!!} . \quad \text{(A10)}$$

Substituting these coefficients into equation (A6), we arrange the series as

$$R = \frac{2}{\pi} b^2 \left[\sum_{k=o}^{\infty} \frac{(2k-1)!!}{(2k+1)(2k)!!} r^{2k+1} + a^2(1-r) \sum_{k=o}^{\infty} \frac{(2k-1)!!}{(2k)!!} r^{2k} \right] \quad (A11)$$

The first series converges to arcsin r, the second to $(1-r^2)^{-1/2}$. Thus

$$R = \frac{2}{\pi} b^2 \left(\arcsin r + a^2 \sqrt{\frac{1-r}{1-r^2}} \right) , \quad (A12)$$

or, renormalizing and simplifying,

$$R_n(r) = \frac{R(r)}{R(1)} = \frac{2}{\pi} \left(\arcsin r + a^2 \sqrt{\frac{1-r}{1+r}} \right) . \quad (A13)$$

Inversion of equation (A13) is easily accomplished by straightforward iterative substitution in

$$r(R_n) = \sin \left(\frac{\pi}{2} R_n - a^2 \sqrt{\frac{1-r}{1+r}} \right) , \quad (A14)$$

which converges rapidly except for $r \cong 1$. The constant a^2 can be determined empirically by an average over the observed correlation function at large lags, where the

true correlation can be assumed to vanish:

$$R_n[r(\tau>>\Delta\tau)] \simeq R_n(0) = \frac{2}{\pi} a^2 . \qquad \text{(A15)}$$

APPENDIX B - FRINGE PARAMETER ESTIMATION

The central problem in interferometer data deduction is the accurate determination of the fringe visibility function from a large number of raw observed values. Each of these values is already an average of the unobservable instantaneous visibility function over a brief interval, and further averaging is generally employed as a first stage of data reduction. But the utility of averaging is limited by the concomitant narrowing of the frequency "window" of observable fringes, which in turn restricts the observable field of view. Hence it is usually necessary to resort to a Fourier transform of a sequence of data to accomplish lengthy integrations; this process can be viewed heuristically as "rotating the fringes" (i.e., shifting the fringe frequency) by a variety of offsets within the fringe-frequency window, followed by averages over the entire time span of the data.

However, frequently - particularly in VLBI observations - the only source regions visible to the interferometer are all within several fringes of each other (though not necessarily near the interferometer phase center). In this case, the observed visibility can be well approximated

by

$$Z(t) = C(t) + i\,S(t) = x_1 \exp\,[i\,(x_2 t + x_3)], \qquad (B1)$$

a functional form very amenable to non-linear least-square fitting. The span of t over which this approximation is valid is restricted only by the requirement that variations in the parameters x_j be negligible. (A similar restriction, of course, applies to the Fourier transform approach.)

For accurate estimation of the parameters x_j, the least-squares technique is advantageous in several respects: the data points need not be equally spaced in time; the use of empirical weights is easily incorporated; variances and covariances are determined concurrently with the parameter estimates; and the estimates are statistically simple. When the observed values of $C(t)$ and $S(t)$ in equation (B1) are all independent, the solution of the least-square problem is particularly tractable and rapidly computable. In this Appendix we give a brief derivation of this solution.

The reader is referred to the statistical literature for a general treatment of the non-linear least-squares problem. Hamilton's (1964) discussion is both clear and comprehensive; adopting his notation, we outline the fitting procedure.

We have $\underline{n}$ observed values $\underline{f}_i^{obs}$ and their $\underline{n}$-by-$\underline{n}$ variance-covariance matrix $\underline{\underline{M}}_f = \{\text{cov}\ (\underline{f}_i^{obs}, \underline{f}_j^{obs})\}$. Each $\underline{f}_i^{obs}$ is to be fitted by a function $\underline{f}_i$ of the $\underline{m}$ variable parameters $\underline{x}_j$. We have also an initial-estimate vector $\underline{\underline{X}}^\circ = \{x_j^\circ\}$ for the parameters. This estimate is refined by solving for the vector $\hat{\underline{\underline{X}}}$ which minimizes the quadratic form

$$Q = (\underline{\underline{F}} - \underline{\underline{A}}\ \hat{\underline{\underline{X}}})'\ \underline{\underline{P}}\ (\underline{\underline{F}} - \underline{\underline{A}}\ \hat{\underline{\underline{X}}})\ , \tag{B2}$$

where $$\underline{\underline{F}} = \left\{ f_i^{obs} - f_i\ (\underline{\underline{X}}^\circ) \right\} \tag{B3}$$

$$\underline{\underline{A}} = \left\{ \frac{\partial f_i}{\partial x_j} \Bigg|_{\underline{\underline{X}}^\circ} \right\}\ , \tag{B4}$$

and $$\underline{\underline{P}} = \sigma^2\ \underline{\underline{M}}_f^{-1}. \tag{B5}$$

The constant $\underline{\sigma}^2$, and thus the absolute scaling of $\underline{\underline{M}}_f$, need not be known; as described later, they can be determined after solving the variational problem.

The solution of this linearized problem is given by

$$\hat{\underline{\underline{X}}} = \underline{\underline{B}}^{-1}\ (\underline{\underline{A}}'\ \underline{\underline{P}}\ \underline{\underline{F}}), \tag{B6}$$

where $$\underline{\underline{B}} = \underline{\underline{A}}'\ \underline{\underline{P}}\ \underline{\underline{A}}, \tag{B7}$$

called the "matrix of normal equations", must be inverted.

The solution vector $\hat{\underline{\underline{X}}}$ is the best-fitting correction to $\underline{\underline{X}}^\circ$. We replace $\underline{\underline{X}}^\circ$ by $\underline{\underline{X}}^\circ + \hat{\underline{\underline{X}}}$ and solve again for a new correction vector; after a number of such iterations, with good fortune, stable values of the parameters obtain and the refinement is said to have converged. Hamilton (1964) discusses techniques for insuring convergence and other topics related to convergence. We assume here that the signal-to-noise ratio in the data is good enough that a well-defined minimum exists in the parameter space.

At each iteration we can evaluate the constant $\underline{\sigma}^2$ according to

$$\sigma^2 = Q / (n-m). \tag{B8}$$

Here $\underline{Q}$ should be calculated from equation (B2), using the solution $\hat{\underline{\underline{X}}}$ obtained from equation (B6). As a computational expedient, however, it is convenient to take $\hat{\underline{\underline{X}}} = 0$ and calculate

$$\hat{\sigma}^2 = \underline{\underline{F}}' \, \underline{\underline{P}} \, \underline{\underline{F}} / (n-m). \tag{B9}$$

This overestimates $\underline{\sigma}^2$, but the effect becomes negligible as convergence is approached.

Having found $\underline{\sigma}^2$ we can then obtain the parameter variance-covariance matrix

$$\hat{\underline{\underline{M}}}_x = \hat{\sigma}^2 \quad \underline{\underline{B}}^{-1}. \tag{B10}$$

The variances determined from this matrix apply to the corrections, but as convergence is approached they give as well the variances of the parameter estimates themselves.

Consider now the particular case described by equation (B1). The observed values are

$$C_i = C(t_i) \text{ and } S_i = S(t_i),\ i = 1, \ldots, N. \tag{B11}$$

We assume these are all independent, and that the variance of both $\underline{C}_i$ and $\underline{S}_i$ is inversely proportional to a weight $\underline{w}_i$. A final assumption fixes the origin of $\underline{t}$, and establishes the epoch to which the phase parameter $\underline{x}_3$ refers:

$$\sum_{i=1}^{N} w_i t_i = 0 \tag{B12}$$

The independence of the $\underline{C}_i$ from the $\underline{S}_i$ allows a formal separation of the variational problem in equation (B2):

$$\begin{aligned} Q = \quad & (\underline{\underline{F}}_C - \underline{\underline{A}}_C \hat{\underline{\underline{X}}})' \ \underline{\underline{P}} \ (\underline{\underline{F}}_C - \underline{\underline{A}}_C \hat{\underline{\underline{X}}}) \\ + \quad & (\underline{\underline{F}}_S - \underline{\underline{A}}_S \hat{\underline{\underline{X}}})' \ \underline{\underline{P}} \ (\underline{\underline{F}}_S - \underline{\underline{A}}_S \hat{\underline{\underline{X}}}), \end{aligned} \tag{B13}$$

where, using complex notation for brevity,

$$\underline{\underline{F}}_c + i\underline{\underline{F}}_s = \left\{ (C_i + iS_i) - X_i^\circ \exp\left[i\left(x_2^\circ t_i + x_3^\circ\right)\right] \right\} , \tag{B14}$$

$$\underline{\underline{A}}_c + i\underline{\underline{A}}_s = \left\{ \begin{array}{l} \exp\left[i\left(x_2^\circ t_i + x_3^\circ\right)\right] \\ i\, t_i x_1^\circ \exp\left[i\left(x_2^\circ t_i + x_3^\circ\right)\right], \\ i x_1^\circ \exp\left[i\left(x_2^\circ t_i + x_3^\circ\right)\right] \end{array} \right\} \tag{B15}$$

and the common weight matrix is

$$\underline{\underline{P}} = \left\{ w_i\, \delta_{ik} \right\} . \tag{B16}$$

The matrix of normal equations corresponding to equation (B13) is diagonal (with the aid of eq. [B12]):

$$\underline{\underline{B}} = \underline{\underline{A}}_c' \underline{\underline{P}} \underline{\underline{A}}_c + \underline{\underline{A}}_s' \underline{\underline{P}} \underline{\underline{A}}_s = \left\{ b_j\, \delta_{jk} \right\} , \tag{B17}$$

and can be inverted by inspection, and the solution vector

$$\hat{\underline{\underline{X}}} = \underline{\underline{B}}^{-1} \left(\underline{\underline{A}}_c' \underline{\underline{P}} \underline{\underline{F}}_c + \underline{\underline{A}}_s' \underline{\underline{P}} \underline{\underline{F}}_s \right) \tag{B18}$$

has the simple form given explicitly below, where for clarity we drop the superscript on the components of $\underline{\underline{X}}^\circ$, write the components of $\hat{\underline{\underline{X}}}$ as $\underline{\Delta x_j}$, and omit the limits on the summations over $\underline{i} = 1, \ldots, \underline{N}$.

Define first the intermediate quantities

$$\alpha_i = C_i \cos(x_2 t_i + x_3) + S_i \sin(x_2 t_i + x_3) \quad \text{(B19)}$$

$$\beta_i = -C_i \sin(x_2 t_i + x_3) + S_i \cos(x_2 t_i + x_3). \quad \text{(B20)}$$

Then

$$\Delta x_1 = \Sigma w_i \alpha_i / \Sigma w_i - x_i, \quad \text{(B21)}$$

$$\Delta x_2 = \Sigma w_i t_i \beta_i / (x_i \Sigma w_i t_i^2), \quad \text{(B22)}$$

$$\Delta x_3 = \Sigma w_i \beta_i / (x_i \Sigma w_i). \quad \text{(B23)}$$

Finally, following equations (B9) and (B10)

$$\hat{\sigma}^2 = \Sigma w_i [\alpha_i^2 + \beta_i^2 - 2\alpha_i x_1 + x_1^2] / (2N-3), \quad \text{(B24)}$$

and the variances of the $\underline{\Delta x_j}$ are

$$\sigma^2 [\Delta x_1] = \hat{\sigma}^2 / \Sigma w_i, \quad \text{(B25)}$$

$$\sigma^2 [\Delta x_2] = \hat{\sigma}^2 / (x_1^2 \Sigma w_i t_i^2), \quad \text{(B26)}$$

$$\sigma^2 [\Delta x_3] = \hat{\sigma}^2 / (x_1^2 \Sigma w_i); \quad \text{(B27)}$$

the covariances among the $\underline{\Delta x_j}$ vanish and the corrections

are thus uncorrelated.

In considering the statistical properties of the least-square parameter estimates, we will assume that the errors in the estimates are sufficiently small that the model in equation (B1) is linear over a range of several standard deviations in each parameter. (In fact this comment applies only to $\underline{x}_2$ and $\underline{x}_3$, since $\underline{x}_1$ is linear without approximation. Note that equation (B21) estimates $\underline{x}_1$ directly from the values of $\underline{x}_2$ and $\underline{x}_3$ at the previous iteration; the estimate is simply the Fourier component of the $\underline{C}_i$ and $\underline{S}_i$ at frequency $\underline{x}_2$, projected onto phase $\underline{x}_3$.) Under this assumption the estimates $\underline{x}_j$ are unbiased in the following sense: if the data are given by the functions $\underline{C(t)}$ and $\underline{S(t)}$ of equation (B1), plus zero-mean noise, then the expected values of the estimates $\underline{x}_j$ at convergence are equal to the parameters $\underline{x}_j$ of equation (B1).

Heretofore only two rather general assumptions regarding the distribution of the errors in the data have been necessary: the first moment must vanish, and the second moment must be finite. In VLBI data, however, we can infer from the central limit theorem that the errors are normally distributed, since each datum is an average of a very large number of binomially-distributed one-bit correlations. This leads to the important result that the $\underline{\Delta x}_j$ - and thus

the $\underline{x}_j$ as well - are also normally distributed.

It must be noted that no constraints are imposed in the fitting process to insure "reasonable" parameter estimates; in particular, the amplitude $\underline{x}_1$ may be negative. If we require positive amplitudes we may use the absolute value of $\underline{x}_1$, adding half a turn to the phase $\underline{x}_3$ when $\underline{x}_1$ is negative. In so doing, however, we sacrifice the statistical simplicity of the least-squares result, for the absolute value of $\underline{x}_1$ is neither normally distributed nor an unbiased estimator of the amplitude.

More specifically, letting $\underline{A}$ and $\underline{\sigma}^2$ represent the mean and variance of the normal distribution of $\underline{x}_1$ ($\underline{A}$ is thus the "true" amplitude in eq. [B1]), it can be shown that $\underline{y} = |\ \underline{x}_1\ |$ has probability density function

$$f_y(y) = \begin{cases} 0, & y \leq 0 \\ \frac{\sqrt{2/\pi}}{\sigma}\ e^{-(A^2+y^2)/2\sigma^2}\ \cosh\left(\frac{Ay}{\sigma^2}\right), & y > 0\ . \end{cases} \qquad \text{(B28)}$$

An unbiased maximum-likelihood estimator for $\underline{A}$ can be obtained from this distribution as the solution of

$$\hat{A} = y \tanh\left(\frac{\hat{A}y}{\sigma^2}\right)\ . \qquad \text{(B29)}$$

but for practical work a simpler estimator, also unbiased,

is expedient:

$$\hat{A}^2 = y^2 - \sigma^2 = x_1^2 - \sigma^2. \qquad \text{(B30)}$$

Equations (B29) and (B30) may be compared with Moran's (1976) equations (5.5.47) and (5.5.48) for estimating $\underline{A}$ from a set of Rice-distributed observations.

APPENDIX C - CALIBRATION

This appendix describes the calibration of spectral VLBI observations. The discussion is specific to the Mark II system, but assumptions about the type of spectrum observed are avoided; occasional special cases which apply only to emission or absorption spectra are identified as such. Mathematically the treatment is heuristic rather than rigorous.

The entire calibration scheme is introduced at the outset, followed by a description of its individual parts. Several methods of obtaining the frequency-dependent amplitude calibration are considered in detail. Finally, the specific approach adopted for the observations discussed in the main text is outlined.

The primary input to the calibration procedure is the interferometer spectrum X_ν, obtained by first correcting the raw normalized crosscorrelation function for the distortion introduced by the one-bit digitization in the recording system, and then Fourier transforming into the spectral domain. (The distortion correction, treated in detail in Appendix A, is generally a nonlinear operation and must precede the Fourier transform; for the crosscorrelation function, as is well known, a linear approximation is often satisfactory, and can be combined with the calibration

described here.)

The calibration procedure applies further corrections for a variety of instrumental effects, deriving the visibility spectrum Γ_ν according to the fundamental equation

$$\Gamma_\nu = \sqrt{\left[\frac{T_R+\bar{T}_A}{T_{A\nu}}\right]_1\left[\frac{T_R+\bar{T}_A}{T_{A\nu}}\right]_2} \cdot \frac{e^{-i(\psi_{\nu_2}-\psi_{\nu_1})}}{\sqrt{f_{\nu_1} f_{\nu_2}}} \cdot$$

$$b_r e^{-i2\pi\nu(\Delta\tau_0+\Delta\tau_1)} \cdot b_\phi \cdot X_\nu \,. \qquad \text{(C1)}$$

In the following paragraphs each factor of equation (C1) is considered in turn. We describe the effect requiring correction, introduce the notation, suggest heuristically the algebraic form of the correction, and, finally, discuss the determination of numerical values. The subscripts 1 and 2 in equation (C1) will always refer to the two antennas forming a particular interferometer.

The presence of uncorrelated receiver noise in the correlator input signals dilutes the correlation between the source signals, requiring a rescaling specified in the first factor of equation (C1). The two contributions to the input signals are represented by, respectively, the receiver noise temperature T_R (assumed constant over the observed band) and the source antenna temperature spectrum $T_{A\nu}$. At each antenna, only the fraction $T_{A\nu}/(T_R + \bar{T}_A)$ of

the power in the recorded signal is due to the source, where we have approximated the source contribution to the total system noise by the mean $\overline{T}_A$. The geometric mean in equation (C1) thus removes this effect from the interferometer spectrum. The determination of this factor can be accomplished in several ways, and we defer until later a detailed discussion and comparison of these methods.

Besides adding noise, the receiving equipment at each station also impresses frequency-dependent amplitude and phase characteristics upon the recorded signals. Unlike the receiver noise, which is dominated by the first mixer or amplifier, this "bandpass spectrum" is controlled by the final narrow-band video-frequency filter. We denote this (voltage) spectrum by $\sqrt{f_\nu} e^{i\psi_\nu}$, in which

$$< f_\nu > \; = \; 1. \tag{C2}$$

The form adopted is convenient because it allows us to write the single-antenna power spectrum as

$$A_\nu \; \propto \; (T_R + T_{A\nu}) \; f_\nu \; , \tag{C3}$$

a relation we will give more explicitly later. The second factor in equation (C1) removes the bandpass spectra of both stations from the interferometer spectrum. Like the receiver-noise factor discussed previously, the bandpass amplitude spectrum f_ν can be determined by a variety of methods, and we discuss both together below. The differential bandpass phase characteristic $\psi_{\nu_2} - \psi_{\nu_1}$ can only be

determined from interferometer observations of continuum sources, where Γ_ν is independent of ν over the observed band. Since suitable sources are few, and valuable telescope time is expended in observing them, such determinations are perforce occasional, and possible variations in ψ_ν must be ignored.

The third factor in equation (C1) introduces corrections for two effects stemming from the digital recording technique. First, the "fringe rotation" prior to correlation must be implemented digitally. In the Mark II VLBI system a crude but digitally tractable three-step approximation to the cisoidal functions is used, which reduces the correlation by 22%. (Reid [1975] gives a lucid derivation of this effect.) The factor $b_r = 1.28$ removes the effect of this decorrelation.

The digital recording technique also confines the interferometer delay to integral multiples of a 250-ns "bit". This discrete delay tracking introduces a delay error as large as half a bit, shifting the delay center of the crosscorrelation function and, by an elementary property of the Fourier transform, applying a phase "twist" $e^{i2\pi\nu\Delta\tau_0}$ to the interferometer spectrum, where $\Delta\tau_0$ is the delay error. It is important to note that while $\Delta\tau_0$ never exceeds the sampling interval (250 ns) appropriate to the maximum 2 MHz bandwidth of the Mark II system, the video

frequency ν is restricted to the bandwidth actually observed. Hence in narrow-bandwidth observations the product $\nu\Delta\tau_0$ never exceeds a small fraction of a turn, and the twist can safely be ignored.

In addition to the rapidly-changing delay error $\Delta\tau_0$, a slowly-changing or constant delay error $\Delta\tau_1$ occurs, caused by inaccuracies in the baseline or source coordinates, or, more importantly, in the offset between the atomic clocks. While the corrections for both rapidly- and slowly-changing delay errors have been combined in equation (C1) for simplicity, in practice quite different treatments are necessary. Removal of the twist $\nu\Delta\tau_0$ must precede any averaging, and this operation in fact is often combined with the Fourier transformation. The value of $\Delta\tau_0$ is well known from the delay calculation. In contrast, the slowly-changing twist $\nu\Delta\tau_1$ need not be removed until after extensive averaging; and since $\Delta\tau_1$ can only be determined to high accuracy by fitting such a twist in a continuum-source observation, extensive averaging is in fact a necessity. In this connection we note that the differential bandpass phase spectrum $\psi_{\nu_2}-\psi_{\nu_1}$ discussed earlier need only be determined to within a constant slope.

The factor b_ϕ, finally, represents a correction for the decorrelating effects of interferometer phase fluctuations. At low frequencies (below about 1 GHz) the fluctuations are

caused by ionospheric scintillation; at higher frequencies variations between the independent frequency standards become dominant. Both effects are independent of frequency within the observed band, but may be time-dependent. Unfortunately b_ϕ cannot be determined accurately. If a point source can be observed (generally a risky assumption), and time variations are ignored, we can obtain an empirical estimate. And "crossing points" in the (u, v) plane, where two different interferometers sample the same spatial frequency components, provide ratios between the b_ϕ factors for different baselines.[1]

We now discuss in detail the determination of the receiver-noise and bandpass-amplitude corrections, which we deferred earlier. We consider a combined single-antenna amplitude correction factor

---

[1] In the observations described in the main text, neither a point source nor crossing points were available, and it was necessary to assume $b_\phi = 1$. Since the important results derived there were shown to be insensitive to overall scaling errors, the primary uncertainty introduced by this assumption concerns inter-baseline variations in the short integrations. Extensive tests of interferometer coherence suggest that such variations do not exceed about 10%.

$$F_\nu = \frac{T_R + \bar{T}_A}{f_\nu T_{A\nu}} ; \qquad (C4)$$

the geometric mean of two such factors will give the frequency-dependent part of the amplitude calibration in equation (C1). To determine F_ν we must resort to auxiliary observations, in particular to the single-antenna spectrum A_ν, which is obtained from the raw normalized autocorrelation function as is X_ν from the crosscorrelation function. (No approximation of the distortion correction is possible in this case, however.)

Since A_ν is the Discrete Fourier Transform of a normalized autocorrelation function, we can assert immediately that

$$\langle A_\nu \rangle = 1 ; \qquad (C5)$$

as specified in equation (C2), a similar scaling applies to f_ν. Defining explicitly the mean antenna temperature $\bar{T}_A$ introduced earlier,

$$\langle f_\nu T_{A\nu} \rangle = \bar{T}_A , \qquad (C6)$$

we obtain instead of equation (C3)

$$A_\nu = \frac{T_R + T_{A\nu}}{T_R + \bar{T}_A} f_\nu . \qquad (C7)$$

An important special case of equation (C7) occurs in an off-source observation, where $T_{A\nu} = \bar{T}_A = 0$:

$$A_\nu^{OFF} = f_\nu . \qquad (C8)$$

The most straightforward estimate of F_ν is apparent from equations (C7) and (C8):

$$F_\nu = \left(A_\nu - \frac{T_R}{T_R + \overline{T}_A} A_\nu^{OFF}\right)^{-1} . \qquad (C9)$$

An approximate form of equation (C9) is often used, valid for the case $\overline{T}_A \ll T_R$:

$$F_\nu \simeq \left(A_\nu - A_\nu^{OFF}\right)^{-1} . \qquad (C10)$$

Equation (C10) is the basis for the claim that F_ν can be evaluated without the necessity of measuring T_R and $\overline{T}_A$; while the underlying approximation is often satisfactory for narrow, moderately strong emission lines, it is not valid in the case of absorption against a strong continuum. We do not consider this form further.

In a direct application of equation (C9), we use single on- and off-source antenna spectra to determine F_ν for epochs close to those of the antenna spectra. The random error in F_ν is determined by the noisier of the two single spectra. We consider next two methods in which this random error can be reduced substantially by averaging. Both methods separate the two frequency-dependent parts of F_ν in order to take advantage of the invariant <u>shape</u> of $T_{A\nu}$, which is proportional to the source flux-density spectrum. The

bandpass amplitude spectrum f_ν, assumed invariant[2] as well, is first determined accurately by averaging a large number number of off-source antenna spectra (cf. eqn. [C8]). Next, using this low-noise f_ν, we obtain from the set of on-source spectra A_ν an accurate estimate of the receiver-noise dilution factor $T_{A\nu}/(T_R + \bar{T}_A)$. Solving the fundamental equation (C7),

$$\frac{T_{A\nu}}{T_R + \bar{T}_A} = \frac{A_\nu}{f_\nu} - \frac{T_R}{T_R + \bar{T}_A} \quad . \tag{C11}$$

At this point the two methods diverge. In the "spectrum-fit" method, appropriate to emission spectra, each observed A_ν yields a noisy estimate of $T_{A\nu}/(T_R + \bar{T}_A)$ through equation (C11). Instead of relying on measurements of T_R and $\bar{T}_A$, we determine the second term on the right-hand side by averaging A_ν/f_ν in regions of the spectrum where $T_{A\nu} = 0$; i.e., we "remove a baseline". Averaging the individual estimates, we obtain a "template" which gives the shape of the $T_{A\nu}$ spectrum with low noise.

---

[2] Small, slow variations in f_ν are known to occur at a level of a few tenths of a percent. These are safely ignored, but if large variations are seen, then we must revert to using individual off-source spectra, which dominate the noise in the result and thus obviate these advanced methods.

Finally, refined estimates are produced by scaling the template to fit the initial noisy estimates. Thereby we effectively determine the antenna sensitivity from the antenna spectrum. This method is based on a suggestion by Reid (1975).

For absorption spectra the approach just described is inconvenient. We must use measured receiver and antenna temperatures in equation (C11), because $T_{A\nu}$ does not vanish and we have very poor leverage in extracting the sensitivity from the ratio A_ν/f_ν. However, having acknowledged the necessity of measuring the sensitivity factor $T_R/\overline{T}_A$, we achieve a simplification in this calculation. In this "spectrum-scale" method, we recast equation (C11) as

$$\frac{T_{A\nu}}{\overline{T}_A} = \frac{A_\nu}{f_\nu}\left(1 + \frac{T_R}{\overline{T}_A}\right) - \frac{T_R}{\overline{T}_A} \quad , \tag{C12}$$

noting that $T_{A\nu}/\overline{T}_A$ is constant in scale as well as in shape. Each individual measurement of A_ν, with the accompanying value of $T_R/\overline{T}_A$, yields an independent estimate of $T_{A\nu}/\overline{T}_A$. The average of these is a low-noise normalized source spectrum, which, finally, we divide by the appropriate $(1 + T_R/\overline{T}_A)$ to obtain the desired receiver-noise dilution $T_{A\nu}/(T_R + \overline{T}_A)$.

In applying the spectrum-scale method, it should be remembered that $\overline{T}_A$ is a narrowband measurement, over the observed band. A wideband measurement is less noisy, of

course, but must be corrected for the relatively weaker influence of the absorption line.

A secondary benefit of the spectrum-fit and spectrum-scale methods is the opportunity to evaluate the error in the calibration functions and thus in the visibility spectrum. Comparison of the individual off-source spectra with the mean used for f_ν indicates the error level to be expected in the mean. A similar comparison is possible in the spectrum-scale calculation, in which a component of error from the T_R and $\bar{T}_A$ measurements may be added in quadrature. In the spectrum-fit approach, the error estimates of the template fitting procedure can be combined to evaluate the accuracy of the template.

The observations described in the main text were calibrated by the spectrum-scale method. The mean antenna temperatures $\bar{T}_A$ were measured differently at the three stations: at MPIR the aperture efficiency was assumed constant, and a large number of narrowband measures were averaged; wideband measurements at NRAO were corrected using the adopted source spectrum, again assuming constant aperture efficiency; and at OVRO narrowband values were obtained and smoothed. A dual-level noise source was used at OVRO, and difficulty in determining the ratio between levels may have introduced some systematic bias. Random errors in these measurements were not included in the

estimated error of the visibility amplitudes.

The normalized source spectrum obtained from the MPIR data is, not surprisingly, far superior to those from NRAO and OVRO, and was used throughout the calibration procedure. The bias thus introduced, caused by different beamwidths, is not significant.

REFERENCES

Adams, T. F. 1976, B.A.A.S., 8, 497.

——— 1977, Publ. A.S.P., 89, 488.

Allison, A. C. and Dalgarno, A. 1969, Ap. J., 158, 423.

Baker, P. L. and Burton, W. B. 1975, Ap. J., 198, 281.

Burbidge, E. M. and Burbidge, G. R. 1965, Ap. J., 142, 1351.

Burbidge, E. M., Smith, H. E., and Burbidge, G. R. 1978, Ap. J., 219, 400.

Dalgarno, A. and McCray, R. A. 1972, Ann. Rev. Astron. Astrophys., 10, 375.

DeYoung, D. S., Roberts, M. S., and Saslaw, W. C. 1973, Ap. J., 185, 809 (DRS).

Ekers, R. D., van der Hulst, J. M., and Miley, G. K. 1976, Nature, 262, 369 (EHM).

Field, G. B. 1958, Proc. I.R.E., 46, 240.

——— 1971, in Molecules in the Galactic Environment, ed. Gordon, M. A. and Snyder, L. E. (New York: Wiley), p. 21 ff.

Greisen, E. W. 1973a, Ph. D. Thesis, California Institute of Technology.

——— 1973b, Ap. J., 184, 363.

——— 1973c, Ap. J., 184, 379.

Hamilton, W. C. 1964, Statistics in Physical Science (New York: Ronald).

Helmken, H., Delvaille, J. P., Epstein, A., Geller, M. J., Schnopper, H. W., and Jernigan, J. G. 1978, Ap. J., 221, L43.

Högbom, J. A. 1974, Astron. Astrophys. Suppl., 15, 417.

Hughes, M. P., Thompson, A. R., and Colvin, R. S. 1971, Ap. J. Suppl., 23, 323.

Kaplan, S. A. and Pikel'ner, S. B. 1974, Ann. Rev. Astron. Astrophys., 12, 113.

Kellermann, K. I. and Pauliny-Toth, I. I. K. 1968, Ann. Rev. Astron. Astrophys., 6, 417.

Kellermann, K. I., Jauncey, D. L., Cohen, M. H., Shaffer, B. B., Clark, B. G., Broderick, J., Rönnäng, B., Rydbeck, O. E. H., Matveyenko, L., Moiseyev, I., Vitkevitch, V. V., Cooper, B. F. C., and Batchelor, R. 1971, Ap. J., 169, 1.

Kent, S. M. 1978, in preparation.

Knapp, G. R. and Kerr, F. J. 1974, Astron. Astrophys., 35, 361.

Legg, T. H., Broten, N. W., Fort, D. N., Yen, J. L., Bale, F. V., Barber, P. C., and Quigley, M. J. S. 1973, Nature, 244, 18.

Lynds, C. R. and Sobieski, S. 1961, Publ. N.R.A.O., 1, 155.

Lynds, R. 1970, Ap. J., 159, L151.

Middleton, D. 1946, J. Appl. Phys., 17, 778.

Miley, G. K. and Perola, G. C. 1975, Astron. Astrophys., 45, 223 (MP).

Minkowski, R. 1957, in Radio Astronomy, I.A.U. Symposium No. 4, ed. van de Hulst, H. C. (Cambridge: Cambridge University Press), p. 107.

——— 1968, A. J., 73, 836.

Moran, J. M. 1976, Meth. Exp. Phys., 12, pt. C, 228.

Niell, A. E., Kellermann, K. I., Clark, B. G., and Shaffer, D. B. 1975, Ap. J., 197, L109.

Oort, J. H. 1976, Publ. A.S.P., 88, 591.

Pauliny-Toth, I. I. K., Preuss, E., Witzel, A., Kellermann, K. I., Shaffer, D. B., Purcell, G. H., Grove, G. W., Jones, D. L., Cohen, M. H., Moffet, A. T., Romney, J., Schilizzi, R. T., and Rinehart, R. 1976, Nature, 259, 17.

Purcell, G. H. 1973, Ph. D. Thesis, California Institute of Technology.

Radhakrishnan, V., Murray, J. D., Lockhart, P., and Whittle, R. P. J. 1972a, Ap. J. Suppl., 24, 15.

Radhakrishnan, V., Goss, W. M., Murray, J. D., and Brooks, J. W. 1972b, Ap. J. Suppl. 24, 49.

Radhakrishnan, V. and Goss, W. M. 1972, Ap. J. Suppl., 24, 161.

Reid, M. J. 1975, Ph. D. Thesis, California Institute of Technology.

Rubin, V. C., Ford, W. K. Jr., Peterson, C. J., and Oort, J. H. 1977, Ap. J., 211, 693 (RFPO).

Rubin, V. C., Ford, W. K. Jr., Peterson, C. J., and Lynds, C. R. 1978, Ap. J. Suppl., 37, No. 2 (June 1978) (RFPL).

Ryle, M. and Windram, M. D. 1968, M.N.R.A.S., 138, 1 (RW).

Schilizzi, R. T., Cohen, M. H., Romney, J. D., Shaffer, D. B., Kellermann, K. I., Swenson, G. W. Jr., Yen, J. L., and Rinehart, R. 1975, Ap. J., 201, 263.

Serlemitsos, P. J., Smith, B. W., Boldt, E. A., Holt, S. S., and Swank, J. H. 1977, Ap. J., 211, L63.

Shaffer, D. B. and Schilizzi, R. T. 1975, A. J., 80, 753.

Shields, G. A. and Oke, J. B. 1975, Publ. A.S.P., 87, 879.

van den Bergh, S. 1972, J.R.A.S. Canada, 66, 237.

——— 1977, Astron. Nachr., 298, 285.

Van Vleck, J. H. and Middleton, D. 1966, Proc. I.E.E.E., 54, 2.

Wampler, E. J. 1971, Ap. J., 164, 1.

Wilkinson, P. N. 1972, M.N.R.A.S., 160, 305.

Wilkinson, P. N., Readhead, A. C. S., Anderson, Purcell, G. H. 1978, in preparation.

Wittels, J. J., Knight, C. A., Shapiro, I. I., Hinteregger, H. F., Rogers, A. E. E., Whitney, A. R., Clark, T. A., Hutton, L. K., Marandino, G. E., Niell, A. E., Rönnäng, B. O., Rydbeck, O. E. H., Klemperer, W. K., and Warnock, W. W. 1975, Ap. J., 196, 13.

Wolff, R. S., Mitchell, R. J., Charles, P. A., and Culhane, J. L. 1976, Ap. J., 208, 1.